RESEARCH ARTICLE



WILEY

Computational coupled large-deformation periporomechanics for dynamic failure and fracturing in variably saturated porous media

Shashank Menon | Xiaoyu Songo

Department of Civil and Coastal Engineering, University of Florida, Gainesville, Florida, USA

Correspondence

Xiaoyu Song, Department of Civil and Coastal Engineering, University of Florida, Gainesville, FL 32611, USA. Email: xysong@ufl.edu

Funding information

National Science Foundation, Grant/Award Numbers: 1659932, 1944009

Abstract

The large-deformation mechanics and multiphysics of continuous or fracturing partially saturated porous media under static and dynamic loads are significant in engineering and science. This article is devoted to a computational coupled large-deformation periporomechanics paradigm assuming passive air pressure for modeling dynamic failure and fracturing in variably saturated porous media. The coupled governing equations for bulk and fracture material points are formulated in the current/deformed configuration through the updated Lagrangian-Eulerian framework. It is assumed that the horizon of a mixed material point remains spherical and its neighbor points are determined in the current configuration. As a significant contribution, the mixed interface/phreatic material points near the phreatic line are explicitly considered for modeling the transition from partial to full saturation (vice versa) through the mixed peridynamic state concept. We have formulated the coupled constitutive correspondence principle and stabilization scheme in the updated Lagrangian-Eulerian framework for bulk and interface points. We numerically implement the coupled large deformation periporomechanics through a fully implicit fractional-step algorithm in time and a hybrid updated Lagrangian-Eulerian meshfree method in space. Numerical examples are presented to validate the implemented stabilized computational coupled large-deformation periporomechanics and demonstrate its efficacy and robustness in modeling dynamic failure and fracturing in variably saturated porous media.

KEYWORDS

fracture, large deformation, periporomechanics, phreatic line, porous media, updated Lagrangian

1 INTRODUCTION

The large-deformation mechanics and multiphysics of deformable porous geomaterials (clay and sand) and biomaterials (human tissues and bone) are significant in engineering and science (e.g., geohazards and biomechanics). 1-7 The coupled large deformation and fluid flow/cracking can compromise the integrity of civil infrastructure and could damage human tissues under certain circumstances. 8-11 For instance, faulting propagation triggered by earthquake involves large deformation and multiphysics in geomaterials. 12-15 Landslides and landfill slope failure could be triggered by large deformation, multiphysics processes, or cracking in geomaterials. 16-18 Computational coupled poromechanics is an essential tool in studying the mechanics and physics of such continuous or fracturing porous materials under static and dynamic loads. 2,19-21 Coupled unsaturated periporomechanics 22-26 is a strong nonlocal reformulation of classical coupled local poromechanics²⁷⁻²⁹ through the peridynamic effective force state^{22,30,31} and stabilized multiphase correspondence principle.^{25,32} The coupled governing equations, including the motion equation and mass balance equation, are formulated in terms of integral-differential equations (integration in space and differentiation in time) in lieu of partial differential equations.²⁴ Through the stabilized multiphase correspondence principle, classical constitutive models and physical laws can be incorporated in periporomechanics for modeling the coupled deformation, fracturing, and fluid flow processes in porous media under static and dynamic loads.²⁵ These salient features of periporomechanics make it a legitimate method for modeling coupled static and dynamic large-deformation mechanics and physics of continuous or fracturing porous media. We note that the coupled periporomechanics has been formulated using the total Lagrangian-Eulerian framework.²⁴ In Reference 33, the authors formulated an updated-Lagrangian periporomechanics framework for modeling extreme large-deformation in unsaturated porous media under drained conditions (i.e., uncoupled). As a new contribution, in this article, we propose a fully coupled large-deformation periporomechanics paradigm in the updated Lagrangian-Eulerian framework for modeling dynamic failure and fracturing in variably saturated porous media. In this new framework, the phreatic interface/line^{29,34} is explicitly considered through the mixed peridynamic state concept.

To incorporate the classical constitutive models for porous media into this new coupled periporomechanics paradigm, we reformulate the original multiphase constitutivecorrespondence principle²² in the updated Lagrangian–Eulerian framework. It has been demonstrated in Reference 25 that the multiphase correspondence principle in the total Lagrangian–Eulerian periporomechanics framework has a zero-energy mode instability issue. In Reference 33 we have also shown that the single-phase correspondence principle for the extreme large-deformation periporomechanics formulated in the updated Lagrangian–Eulerian framework inherits the zero-energy mode instability. The authors adopted the so-called sub-horizon concept to remove the zero-energy mode associated with the correspondence principle. However, this method is computationally demanding because a sub-horizon will need to be defined for each bond in its horizon (see Reference 33 for details). In this study, we first demonstrate that the coupled updated Lagrangian–Eulerian periporomechanics also inherits the zero-energy mode issue (see Section 2.3). To reduce the computational cost, we adopt the multiphase stabilization scheme formulated in Reference 25 to resolve the zero-energy mode instability. We refer to the literature for a thorough review of the remedies for circumventing the zero-energy mode associated with the peridynamic correspondence principle (e.g., References 25,32,33,35, among others).

The interface between a saturated zone and an unsaturated zone in variably saturated porous media is called the phreatic interface/line. 9.36 The porous material across the phreatic line has different mechanical and physical properties because of the variation of degree of saturation across the phreatic line. We note that the phreatic line has not been explicitly considered in the previously formulated saturated/unsaturated periporomechanics models. For a mixed material point near the phreatic line, its neighboring material points can be in either a saturated or unsaturated zone. Therefore, to simulate variably saturated soils with a phreatic line using coupled periporomechanics, the material points near the phreatic line should be treated as composite material points. As a significant contribution and novelty, in this study, the mixed interface/phreatic material points near the phreatic line are explicitly considered for better modeling the transition from partially to fully saturated states (vice versa) of porous media through the mixed peridynamic state concept. Specifically, the peridynamic state (e.g., effective force state and fluid flow state) at the material point across the interface line is decomposed into two states, that is, saturated and unsaturated states (see Section 2.2 for details). Following the lines in the stabilization scheme for the bulk mixed material point (i.e., material points and their neighboring points in either fully saturated or unsaturated zones), we have formulated the coupled constitutive correspondence principle and its stabilization scheme for the phreatic interface material points in the updated Lagrangian–Eulerian framework.

We numerically implement the coupled large deformation periporomechanics through a fully implicit fractional-step algorithm in time²⁴ and a hybrid updated Lagrangian–Eulerian meshfree method in space with Open MPI³⁷ for high-performance computing. We refer to the classical literature for technical discussions on monolithic and fractional-step/staggered algorithms for numerically implementing the coupled poromechanics in time (e.g., References 38-42, among others). It is assumed that the horizon of a mixed material point remains spherical, and its neighbor points are determined in the current configuration. In line with this assumption, in the numerical implementation, the neighboring material point list of a material point updated at time step n is used for the computation at time

step n + 1. The coupled periporomechanics is computationally more demanding than other continuum-based computational methods such as the finite element method (FEM) and XFEM for modeling porous media. 1,2,19,20 We refer to the literature for coupling peridynamics with FEM for modeling porous media (e.g., References 43,44 and others) and the mixed FEMs for large deformation in unsaturated porous media (e.g., References 2,21,45 and others). Numerical examples are presented to validate the implemented stabilized coupled large-deformation periporomechanics and demonstrate its efficacy and robustness in modeling dynamic failure and fracturing in partially saturated porous media.

The original contributions of this article include (i) the mathematical formulation of a fully coupled large-deformation periporomechanics paradigm through the updated Lagrangian–Eulerian framework, (ii) the explicit treatment of interface material points as a composite point through the mixed peridynamic state concept, (iii) the formulation of the coupled constitutive correspondence principle in the updated Lagrangian–Eulerian framework and its stabilization scheme through an energy method, and (iv) the implementation of the formulated large-deformation periporomechanics paradigm through an implicit-implicit fractional step algorithm in time and a hybrid updated Lagrangian-Eulerian meshfree method in space. For sign convention, the assumption in continuum mechanics is followed, that is, for the solid skeleton, tensile force/stress is positive, and compression is negative. For fluid pressure, compression is positive, and tension is negative.

2 | COUPLED LARGE-DEFORMATION UNSATURATED PERIPOROMECHANICS

We present the mathematical formulation of the coupled large-deformation periporomechanics in the updated Lagrangian–Eulerian framework for fracturing unsaturated porous media assuming passive air pressure. The phreatic interface points are explicitly considered in this new framework through the mixed peridynamic state concept. In line with the total Lagrangian–Eulerian periporomechanics, it is assumed that a porous material body can be represented by a finite number of mixed material points that are endowed with two kinds of degrees of freedom, that is, displacement and fluid pressure. In the current/deformed configuration, a mixed material point has poromechanical and physical interactions with all mixed material points within its neighborhood \mathcal{H} , that is, the family. Here \mathcal{H} is a spherical domain around a material point \mathbf{x} with radius δ , called horizon in periporomechanics, in the current configuration. In the updated Lagrangian–Eulerian formulation, it is assumed that the horizon remains the same. In line with this assumption, the family \mathcal{H} of a mixed material point \mathbf{x} in the current configuration is determined by

$$\mathscr{H} := \{ \mathbf{x}' | \mathbf{x}' \in \mathscr{B}, 0 \le \|\underline{\zeta}\| \le \delta \}, \tag{1}$$

where \mathcal{B} denotes a porous material body and $\underline{\zeta} = x' - x$ is the mixed (multiphase) bond between material points x and x'. With this assumption, the extreme distortion of the horizon for large deformation of the solid skeleton in the total Lagrangian formulation can be avoided. Indeed this assumption is consistent with the Eulerian formulation of peridynamics for solids in Reference 46. However, the material point of the solid skeleton is described by its motion, and the fluid phase is described by the relative Eulerian coordinate referring to the solid skeleton. Thus, the mixed material points in the horizon of a material point x evolves with time in the large deformation regime.

Figure 1 presents the schematics of the initial configuration, current/deformed configuration, and future configuration of a porous material body. We note that all variables refer to the current/deformed configuration in the formulation presented in this section instead of the initial/undeformed configuration as in the total Lagrangian–Eulerian periporomechanics. For conciseness of notations, in the current configuration the peridynamic state variable without a prime denotes the variable evaluated at \mathbf{x} on the associated bond $\underline{\zeta} = \mathbf{x}' - \mathbf{x}$ and the peridynamic state variable with a prime stands for the variable evaluated at \mathbf{x}' on the associated bond $\underline{\zeta}' = \mathbf{x} - \mathbf{x}'$, for example, $\mathcal{F} = \mathcal{F}[\mathbf{x}]\langle \mathbf{x}' - \mathbf{x}\rangle$ and $\mathcal{F}' = \mathcal{F}[\mathbf{x}']\langle \mathbf{x} - \mathbf{x}'\rangle$. In what follows, we first present the governing equations and the coupled correspondence principle in the updated Lagrangian–Eulerian framework for a mixed material point (and its neighbor material points) (i.e., the bulk material point) in the unsaturated or fully saturated domain. Second, we formulate the governing equations and the coupled correspondence principle for the phreatic material point through the mixed peridynamic state concept. Third, we present the stabilization scheme for the phreatic material point since the stabilization scheme for a bulk material point is a special case, followed by a brief discussion of the material models and physical laws in the new framework.

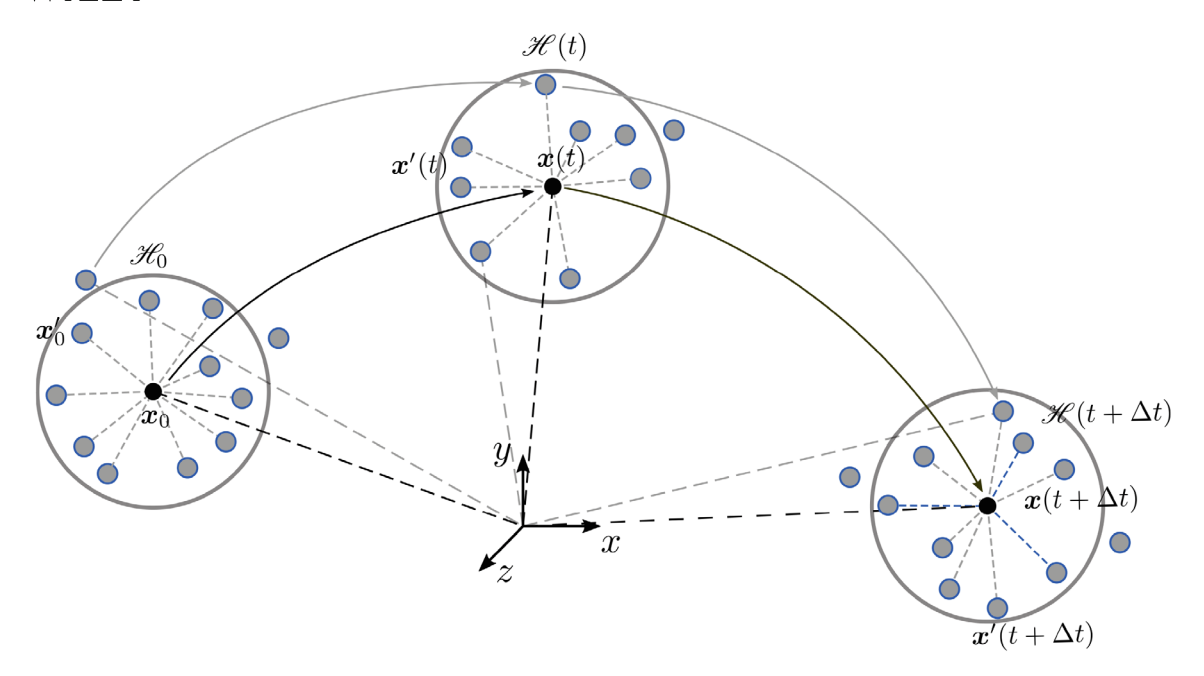


FIGURE 1 Kinematics of the mixed solid skeleton and pore fluid material points in the updated Lagrangian–Eulerian formulation: Initial configuration, current/deformed configuration, and future configuration.

2.1 | Formulation of a material point in unsaturated or fully saturated zones

We define the deformation vector state $\underline{y} = y' - y$ as the mapping of $\underline{\zeta}$ from the current configuration to the next configuration in which \underline{y}' and \underline{y} represent the same material points of the solid skeleton in the next configuration.

In line with the total Lagrangian formulation of periporomechanics, $^{23-25}$ the equation of motion at material point \boldsymbol{x} in the current configuration reads

$$\rho \ddot{\boldsymbol{u}} = \int_{\mathcal{X}} (\overline{\underline{\mathcal{T}}} - S_r \underline{\mathcal{T}}_w) - (\overline{\underline{\mathcal{T}}}' - S_r' \underline{\mathcal{T}}_w') \, d\mathcal{V}' + \rho \boldsymbol{g}, \tag{2}$$

where $\overline{\mathcal{F}}$ and $\overline{\mathcal{F}}'$ are the effective force vector states at \boldsymbol{x} and \boldsymbol{x}' , respectively, $\underline{\mathcal{F}}_w$ and $\underline{\mathcal{F}}'_w$ are the fluid force vector states at \boldsymbol{x} and \boldsymbol{x}' , respectively, S_r and S_r' are the degrees of saturation at \boldsymbol{x} and \boldsymbol{x}' , respectively, $d\mathcal{F}'$ is the volume of the neighboring material point in the current configuration, $\ddot{\boldsymbol{u}}$ is the acceleration vector, ρ is the density of the mixture, and \boldsymbol{g} is the gravity acceleration. Assuming weightless pore air, the density of the mixture ρ reads

$$\rho = \rho_{\rm S}(1 - \phi) + S_r \rho_w \phi,\tag{3}$$

where ρ_s is the intrinsic density of the solid, ρ_w is the intrinsic density of water, and ϕ is the porosity in the current configuration. The balance of mass at material point \boldsymbol{x} in the current configuration reads

$$\phi\left(\frac{S_r}{K_w} + \frac{\partial S_r}{\partial p_w}\right) \frac{\mathrm{d}p_w}{\mathrm{d}t} + S_r \dot{\mathcal{V}}_s + \int_{\mathcal{X}} \left(\underline{\mathcal{Q}} - \underline{\mathcal{Q}}'\right) \,\mathrm{d}\mathcal{V}' + Q_s = 0,\tag{4}$$

where $\dot{\gamma}_s$ is the solid volume change rate at x, \underline{Q} , and \underline{Q}' are the fluid flow states at x and x', respectively, p_w is the pore water pressure, Q_s is a source term, and K_w is the bulk modulus of water.

For a fracture material point, similar to (2) the equation of motion can be written as

$$\rho \ddot{\boldsymbol{u}} = \int_{\mathcal{U}} \left(\underline{\overline{\mathcal{T}}} - \underline{\overline{\mathcal{T}}}' \right) \, d\mathcal{V}' - \int_{\mathcal{U}} \left(S_l \underline{\mathcal{T}}_l - S_l' \underline{\mathcal{T}}_l' \right) \, d\mathcal{V}' + \rho \boldsymbol{g}, \tag{5}$$

-WILEY

where

$$S_{l}\underline{\mathcal{T}}_{l} = \begin{cases} S_{r,f}\underline{\mathcal{T}}_{f} & \text{for a fracture point,} \\ S_{r}\underline{\mathcal{T}}_{w} & \text{otherwise.} \end{cases}$$
 (6)

The mass balance equation in the fracture space can be written as

$$\frac{\partial S_{rf}}{\partial p_w} \frac{\partial p_w}{\partial t} + \int_{\mathcal{H}} \left(\underline{\mathcal{Q}}_f - \underline{\mathcal{Q}}_f' \right) d\mathcal{V}' - \mathcal{Q}_s = 0, \tag{7}$$

where $\underline{\mathscr{Q}}_f$ are the fracture fluid flow states at material points \boldsymbol{x} and $\boldsymbol{x'}$, respectively. In the fully saturated regime, $S_r = 1$ and $\partial S_r / \partial p_w = 0$. Therefore, Equations (2), (4), (5), and (7) naturally degenerate into the equations under saturated conditions. In what follows, we cast the coupled corresponding principle in the updated Lagrangian–Eulerian framework.

2.1.1 | Coupled corresponding principle in the updated Lagrangian–Eulerian framework

The rate of strain energy of the solid skeleton assuming elastic deformation in the updated Lagrangian–Eulerian periporomechanics reads²²

$$\dot{\mathcal{W}} = \int_{\mathcal{Q}} \int_{\mathcal{Q}} \underline{\mathcal{G}}_i \, \underline{\dot{\mathcal{Y}}}_i \, d\mathcal{V}' d\mathcal{V} \,. \tag{8}$$

Next, we express the rate of strain energy of the solid skeleton in terms of effective stress and the rate of deformation. The velocity gradient³³ can be written as

$$\mathcal{L} = \left(\int_{\mathcal{X}} \underline{\omega} \, \underline{\dot{\mathbf{Y}}} \otimes \underline{\zeta} \, d\mathcal{V}' \right) \mathcal{K}^{-1}, \tag{9}$$

where ω is the weighting function and \mathcal{K} is the spatial shape tensor in the current configuration

$$\mathcal{K} = \int_{\mathcal{X}} \underline{\omega} \, \underline{\zeta} \otimes \underline{\zeta} \, d\mathcal{V}'. \tag{10}$$

Given (9), the rate of nonlocal deformation reads

$$\mathcal{D} = \frac{1}{2}(\mathcal{L} + \mathcal{L}^T). \tag{11}$$

The rate of the strain energy of the solid skeleton assuming elastic deformation in classical poromechanics can be written as^{22,30}

$$\dot{\mathcal{W}} = \int_{\mathcal{B}} \overline{\sigma}_{ij} \mathcal{D}_{ij} \, d\mathcal{V} ,$$

$$= \int_{\mathcal{B}} \overline{\sigma}_{ij} \left(\int_{\mathcal{H}} \underline{\omega} \underline{\dot{\mathcal{Y}}}_{i} \underline{\zeta}_{k} \, d\mathcal{V}' \right) \mathcal{K}_{kj}^{-1} \, d\mathcal{V} ,$$

$$= \int_{\mathcal{B}} \left(\int_{\mathcal{H}} \underline{\omega} \underline{\dot{\mathcal{Y}}}_{i} \underline{\zeta}_{k} \, d\mathcal{V}' \right) \mathcal{K}_{kj}^{-1} \overline{\sigma}_{ji} \, d\mathcal{V} ,$$

$$= \int_{\mathcal{B}} \int_{\mathcal{B}} \underline{\omega} \underline{\zeta}_{k} \mathcal{K}_{kj}^{-1} \overline{\sigma}_{ji} \underline{\dot{\mathcal{Y}}}_{i} \, d\mathcal{V}' \, d\mathcal{V} ,$$
(12)

where i, j, k = 1, 2, 3.

Then, it follows from (12) and (8) that the effective force state can be related to the effective Cauchy stress tensor as

$$\overline{\underline{\mathcal{T}}} = \underline{\omega} \zeta \mathcal{K}^{-1} \overline{\sigma}. \tag{13}$$

Through the effective force state concept, the fluid force state can be written as

$$\underline{\mathcal{T}}_{w} = \underline{\omega} \zeta \mathcal{K}^{-1}(S_{r} p_{w} \mathbf{1}). \tag{14}$$

The rate from of energy dissipation due to fluid flow in periporomechanics can be written as²²

$$\dot{\mathcal{W}}_{d} = \int_{\mathcal{B}} \int_{\mathcal{B}} \underline{\mathcal{Q}} \, \underline{\Phi} \, d\mathcal{V}', \tag{15}$$

where $\underline{\Phi} = p'_w - p_w$ is the pressure potential state. Similar to (9), the spatial gradient of fluid pressure in the current configuration can be written as^{23,33}

$$\operatorname{grad}(p_w)_i = \operatorname{grad}(\widetilde{\Phi})_i = \left(\int_{\mathscr{X}} \underline{\omega} \, \underline{\Phi} \, \underline{\zeta}_j \, d\mathscr{V}'\right) \mathscr{X}_{ji}^{-1}. \tag{16}$$

The rate form of the energy dissipation due to fluid flow in classical poromechanics²² reads

$$\frac{\dot{\mathcal{W}}}{\mathcal{W}}_{d} = \int_{\mathcal{B}} q_{i} \operatorname{grad}(p_{w})_{i} \, d\mathcal{V},$$

$$= \int_{\mathcal{B}} q_{i} \left(\int_{\mathcal{W}} \underline{\omega} \, \underline{\Phi} \, \underline{\zeta}_{j} \, d\mathcal{V}' \right) \mathcal{K}_{ji}^{-1} d\mathcal{V},$$

$$= \int_{\mathcal{B}} q_{i} \left(\int_{\mathcal{B}} \underline{\omega} \, \underline{\Phi} \, \underline{\zeta}_{j} \, d\mathcal{V}' \right) \mathcal{K}_{ji}^{-1} d\mathcal{V},$$

$$= \int_{\mathcal{B}} \int_{\mathcal{B}} \underline{\omega} q_{i} \mathcal{K}_{ij}^{-1} \underline{\zeta}_{j} \underline{\Phi} \, d\mathcal{V}' d\mathcal{V},$$
(17)

Then, from (17) and (15) the fluid flow state can be written as

$$\underline{\mathcal{Q}} = \underline{\omega} q_i \mathcal{K}_{ij}^{-1} \underline{\zeta}_i. \tag{18}$$

Next, we present the governing equations for a mixed material point at the phreatic interface/line.

2.2 | Formulation of a mixed material point at the phreatic interface/line

The phreatic material point (i.e., the mixed material point near the phreatic interface) could lie in either the unsaturated (vadose) zone or the saturated (phreatic) zone. However, a percentage of the material points in its horizon lies in the vadose zone and the remaining material points lie in the phreatic zone. For this reason, it is hypothesized that the deformation state, effective force state, fluid pressure state, and fluid flow state can be decomposed into two parts through the mixed (double) peridynamic state concept, that is, $\underline{\mathscr{T}}^{(1)}$ and $\underline{\mathscr{T}}^{(2)}$, $\underline{\mathscr{Y}}^{(1)}$ and $\underline{\mathscr{Y}}^{(2)}$, $\underline{\mathscr{Q}}^{(1)}$ and $\underline{\mathscr{Q}}^{(2)}$, and $\underline{\Phi}^{(1)}$ and $\underline{\Phi}^{(2)}$. Figure 2 sketches the periporomechanics representation of the phreatic interface material points for the solid skeleton and fluid phases through the mixed (double) peridynamic state concept.³⁰

It follows from this hypothesis and in line with (8) that the strain energy density at a phreatic mixed material point reads

$$\dot{\mathcal{W}} = \left(\int_{\mathcal{B}} \int_{\mathcal{B}} \overline{\underline{\mathcal{J}}}_{i}^{(1)} \underline{\dot{\mathcal{Y}}}_{i}^{(1)} + \overline{\underline{\mathcal{J}}}_{i}^{(2)} \underline{\dot{\mathcal{Y}}}_{i}^{(2)} \right) d\mathcal{V}' d\mathcal{V}. \tag{19}$$

The two velocity gradient tensors $\mathcal{L}^{(1)}$ and $\mathcal{L}^{(2)}$ at a phreatic mixed material point can be written as

$$\mathscr{Z}^{(1)} = \left(\int_{\mathscr{X}^{(1)}} \underline{\omega} \, \underline{\mathscr{Y}} \otimes \underline{\zeta} \, d\mathscr{V}' \right) \mathscr{K}^{-1}, \tag{20}$$

$$\mathscr{L}^{(2)} = \left(\int_{\mathscr{H}^{(2)}} \underline{\omega} \, \underline{\mathring{\mathcal{Y}}} \otimes \underline{\zeta} \, d\mathscr{V}' \right) \mathscr{K}^{-1}, \tag{21}$$

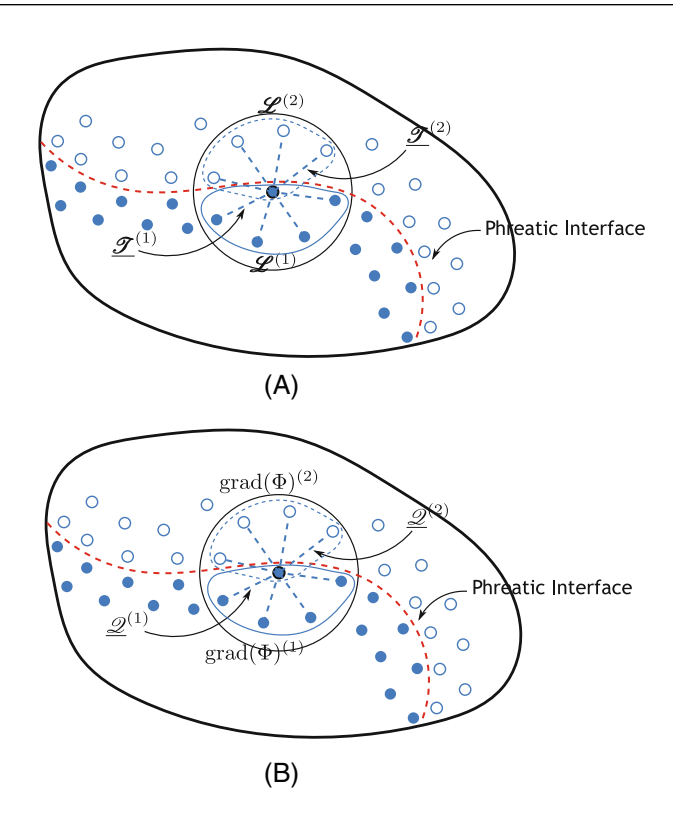


FIGURE 2 Schematics of the phreatic interface material points in periporomechanics for (A) the solid skeleton phase and (B) the pore fluid phase through the mixed (double) peridynamic state concept.

From (11) and (21) we can obtain the rate form of the two deformation tensors at a phreatic material point, that is, $\mathcal{D}^{(1)}$ and $\mathcal{D}^{(2)}$. From a classical constitutive model for the solid skeleton we have two effective stress tensors, that is, $\overline{\sigma}^{(1)}$ and $\overline{\sigma}^{(2)}$. Then, the corresponding strain energy density of (19) in classical unsaturated poromechanics reads

$$\dot{\mathcal{W}} = \dot{\mathcal{W}}^{(1)} + \dot{\mathcal{W}}^{(2)},
= \int_{\mathcal{B}} \overline{\sigma}_{ij}^{(1)} \mathcal{D}_{ij}^{(1)} \, d\mathcal{V} + \int_{\mathcal{B}} \overline{\sigma}_{ij}^{(2)} \mathcal{D}_{ij}^{(2)} \, d\mathcal{V},
= \int_{\mathcal{B}} \left\{ \overline{\sigma}_{ij}^{(1)} \left(\int_{\mathcal{H}^{(1)}} \underline{\omega} \, \underline{\dot{\mathcal{Y}}}_{i} \underline{\zeta}_{k} \, d\mathcal{V}' \right) \mathcal{K}_{kj}^{-1} \right\} \, d\mathcal{V} + \int_{\mathcal{B}} \left\{ \overline{\sigma}_{ij}^{(2)} \left(\int_{\mathcal{H}^{(2)}} \underline{\omega} \, \underline{\dot{\mathcal{Y}}}_{i} \underline{\zeta}_{k} \, d\mathcal{V}' \right) \mathcal{K}_{kj}^{-1} \right\} \, d\mathcal{V},
= \int_{\mathcal{B}} \int_{\mathcal{H}^{(1)}} \left\{ \underline{\omega} \, \underline{\dot{\mathcal{Y}}}_{i} \underline{\zeta}_{k} \mathcal{K}_{kj}^{-1} \overline{\sigma}_{ji} \right\} \, d\mathcal{V}' d\mathcal{V} + \int_{\mathcal{B}} \int_{\mathcal{H}^{(2)}} \left\{ \underline{\omega} \, \underline{\dot{\mathcal{Y}}}_{i} \underline{\zeta}_{k} \mathcal{K}_{kj}^{-1} \overline{\sigma}_{ji} \right\} \, d\mathcal{V}' d\mathcal{V},
= \int_{\mathcal{B}} \int_{\mathcal{H}} \left\{ \underline{\omega} \, \underline{\dot{\mathcal{Y}}}_{i} \underline{\zeta}_{k} \mathcal{K}_{kj}^{-1} \overline{\sigma}_{ji} \right\}^{(1)} \, d\mathcal{V}' d\mathcal{V} + \int_{\mathcal{B}} \int_{\mathcal{H}} \left\{ \underline{\omega} \, \underline{\dot{\mathcal{Y}}}_{i} \underline{\zeta}_{k} \mathcal{K}_{kj}^{-1} \overline{\sigma}_{ji} \right\}^{(2)} \, d\mathcal{V}' d\mathcal{V},
= \int_{\mathcal{B}} \int_{\mathcal{B}} \left(\underline{\omega} \, \underline{\zeta}_{k} \mathcal{K}_{kj}^{-1} \overline{\sigma}_{ji} \right)^{(1)} \underline{\dot{\mathcal{Y}}}_{i}^{(1)} + \left(\underline{\omega} \, \underline{\zeta}_{k} \mathcal{K}_{kj}^{-1} \overline{\sigma}_{ji} \right)^{(2)} \underline{\dot{\mathcal{Y}}}_{i}^{(2)} \, d\mathcal{V}' d\mathcal{V},$$
(22)

where $\dot{W}^{(1)}$ and $\dot{W}^{(2)}$ are strain energy densities associated with the neighboring material points under saturated and unsaturated conditions, respectively.

From (19) and (22), it follows that the effective force states at a phreatic material point can be written as

$$\underline{\underline{\mathscr{T}}}^{(1)} = \left\{ \underline{\omega}\underline{\zeta}\mathscr{K}^{-1}(\overline{\sigma}) \right\}^{(1)}, \tag{23}$$

$$\overline{\underline{\mathscr{T}}}^{(2)} = \left\{ \underline{\omega} \underline{\zeta} \mathscr{K}^{-1}(\overline{\sigma}) \right\}^{(2)}. \tag{24}$$

Through the effective force state concept, the fluid force states at a phreatic material point read

$$\underline{\mathscr{T}}_{w}^{(1)} = \left\{ \underline{\omega} \underline{\zeta} \mathscr{K}^{-1} (S_{r} p_{w} \mathbf{1}) \right\}^{(1)}, \tag{25}$$

$$\underline{\mathscr{T}}_{w}^{(2)} = \left\{ \underline{\omega} \underline{\zeta} \mathscr{K}^{-1} (S_{r} p_{w} \mathbf{1}) \right\}^{(2)}. \tag{26}$$

Then, substituting (23)–(26) into (2) we have the equation of motion at a phreatic material point in terms of the total force states as

$$\rho \ddot{\boldsymbol{u}} = \int_{\mathcal{H}} \left(\underline{\mathcal{T}}^{(1)} + \underline{\mathcal{T}}^{(2)} \right) - \left(\underline{\mathcal{T}}^{\prime(1)} + \underline{\mathcal{T}}^{\prime(2)} \right) \, d\mathcal{V}^{\prime} + \rho \boldsymbol{g}. \tag{27}$$

For the fluid phase, the energy dissipation rate at a phreatic material point through fluid flow can be written as

$$\dot{\mathcal{W}}_{d} = \int_{\mathcal{B}} \int_{\mathcal{B}} \left(\underline{\mathcal{Q}}^{(1)} \, \underline{\Phi}^{(1)} + \underline{\mathcal{Q}}^{(2)} \, \underline{\Phi}^{(2)} \right) \, d\mathcal{V}'. \tag{28}$$

At a phreatic material point, the two fluid pressure gradient vectors can be written as

$$\operatorname{grad}(\widetilde{\Phi})^{(1)} = \left(\int_{\mathcal{X}^{(1)}} \underline{\omega} \, \underline{\Phi} \, \underline{\zeta} \, d\mathcal{V}' \right) \mathcal{K}^{-1}, \tag{29}$$

$$\operatorname{grad}(\widetilde{\Phi})^{(2)} = \left(\int_{\mathcal{H}^{(2)}} \underline{\omega} \, \underline{\Phi} \, \underline{\zeta} \, d\mathcal{V}' \right) \mathcal{H}^{-1}. \tag{30}$$

Given (29) and (30), flux vectors $\mathbf{q}^{(1)}$ and $\mathbf{q}^{(2)}$ can be obtained through the generalized Darcy's law for unsaturated porous media. Then, the energy dissipation rate due to fluid flow at a phreatic material point in classical poromechanics reads

$$\frac{\dot{\overline{W}}_{d}}{\dot{\overline{W}}_{d}} = \frac{\dot{\overline{W}}_{d}^{(1)} + \dot{\overline{W}}_{d}^{(2)}}{\dot{\overline{W}}_{d}} + \frac{\dot{\overline{W}}_{d}^{(2)}}{\dot{\overline{W}}_{d}} + \int_{\mathcal{B}} q_{i}^{(2)} \operatorname{grad}(p_{w})_{i}^{(2)} d\mathcal{V},$$

$$= \int_{\mathcal{B}} \left\{ q_{i}^{(1)} \left(\int_{\mathcal{H}^{(1)}} \underline{\omega} \, \underline{\Phi} \, \underline{\zeta}_{j} \, d\mathcal{V}' \right) \mathcal{K}_{ji}^{-1} \right\} d\mathcal{V} + \int_{\mathcal{B}} \left\{ q_{i}^{(2)} \left(\int_{\mathcal{H}^{(2)}} \underline{\omega} \, \underline{\Phi} \, \underline{\zeta}_{j} \, d\mathcal{V}' \right) \mathcal{K}_{ji}^{-1} \right\} d\mathcal{V},$$

$$= \int_{\mathcal{B}} \int_{\mathcal{H}} \left\{ \underline{\omega} \, \underline{\Phi} \, \underline{\zeta}_{j} \mathcal{K}_{ji}^{-1} q_{i} \right\}^{(1)} d\mathcal{V}' d\mathcal{V} + \int_{\mathcal{B}} \int_{\mathcal{H}} \left\{ \underline{\omega} \, \underline{\Phi} \, \underline{\zeta}_{j} \mathcal{K}_{ji}^{-1} q_{i} \right\}^{(2)} d\mathcal{V}' d\mathcal{V},$$

$$= \int_{\mathcal{B}} \int_{\mathcal{B}} \left(\underline{\omega} \, \underline{\zeta}_{j} \mathcal{K}_{ji}^{-1} q_{i} \right)^{(1)} \underline{\Phi}^{(1)} + \left(\underline{\omega} \, \underline{\zeta}_{j} \mathcal{K}_{ji}^{-1} q_{i} \right)^{(2)} \underline{\Phi}^{(2)} d\mathcal{V}' d\mathcal{V}.$$
(31)

It follows from (31) and (28) that the two fluid flow states at a phreatic material point read

$$\underline{\underline{\mathscr{Q}}}^{(1)} = \left\{ \underline{\omega} \boldsymbol{q} \mathcal{K}^{-1} \underline{\boldsymbol{\zeta}} \right\}^{(1)}, \tag{32}$$

$$\underline{\underline{\mathscr{Q}}}^{(2)} = \left\{ \underline{\omega} \boldsymbol{q} \mathcal{K}^{-1} \underline{\boldsymbol{\zeta}} \right\}^{(2)}. \tag{33}$$

Given (32) and (33) the balance of mass at a phreatic material point can be written as

$$\phi\left(\frac{S_r}{K_w} + \frac{\partial S_r}{\partial p_w}\right) \frac{\mathrm{d}p_w}{\mathrm{d}t} + S_r \sum_{i=1}^2 \mathcal{L}^{(i)} : \mathbf{1} + \int_{\mathcal{X}} \left[\left(\underline{\mathcal{Q}}^{(1)} + \underline{\mathcal{Q}}^{(2)}\right) - \left(\underline{\mathcal{Q}}^{\prime(1)} + \underline{\mathcal{Q}}^{(2)}\right) \right] \, \mathrm{d}\mathcal{V}' + Q_s = 0. \tag{34}$$

In this study, we assume that the fracturing is not across the phreatic interface/line. However, the formulation for fracturing material points across the phreatic line can be achieved following the lines in this section and in Reference 23.

2.3 | Coupled stabilization scheme in the updated Lagrangian-Eulerian framework

In this section, we derive a two-phase stabilization scheme for the two-phase correspondence principle for the phreatic material point formulated in the previous section. Note that the stabilization scheme of the mixed material point completely in either a saturated or an unsaturated domain is a special case of the phreatic material point. For a phreatic material point, the two spatial deformation gradient vectors are written as

$$\mathcal{F}^{(1)} = \int_{\mathcal{X}^{(1)}} \underline{\omega} \, \underline{\mathcal{Y}} \otimes \underline{\zeta} \, d\mathcal{V}' \mathcal{K}^{-1}, \tag{35}$$

$$\mathscr{F}^{(2)} = \int_{\mathscr{H}^{(2)}} \underline{\omega} \, \underline{\mathscr{Y}} \otimes \underline{\zeta} \, \mathrm{d}\mathscr{V}' \mathscr{K}^{-1}. \tag{36}$$

The two residual deformation vector states are written as

$$\underline{\mathscr{R}}^{s,(1)} = \underline{\mathscr{Y}}^{(1)} - \mathscr{F}^{(1)}\underline{\zeta}^{(1)},\tag{37}$$

$$\underline{\mathcal{R}}^{s,(2)} = \underline{\boldsymbol{\mathcal{Y}}}^{(2)} - \mathcal{F}^{(2)}\underline{\boldsymbol{\zeta}}^{(2)}. \tag{38}$$

Substituting (37) and (38) into (35) and (36) generates two null tensors implying that the non-uniform deformation state is not considered by the correspondence principle derived in the last section.³³ The missing non-uniform deformation state is the origin of the zero-energy mode associated with the standard correspondence principle.

The energy method²⁵ is adopted for its computational efficiency. The effective force state with stabilization can be written as

$$\overline{\underline{\mathcal{T}}} = \overline{\underline{\mathcal{T}}}^{(1)} + \overline{\underline{\mathcal{T}}}^{(2)} + \underline{\mathcal{T}}^{(1)}_{s} + \underline{\mathcal{T}}^{(2)}_{s}, \tag{39}$$

where $\underline{\mathcal{T}}_s^{(1)}$ and $\underline{\mathcal{T}}_s^{(2)}$ are the stabilization terms corresponding to $\underline{\overline{\mathcal{T}}}^{(1)}$ and $\underline{\overline{\mathcal{T}}}^{(2)}$, respectively. Next, we determine the two stabilization terms from the energy method. Following References 25,32 we propose that the stabilization force states take the form

$$\underline{\mathcal{J}}_{s}^{(1)} = \beta^{(1)} \underline{\mathcal{R}}^{s,(1)}, \tag{40}$$

$$\underline{\mathscr{T}}_{s}^{(2)} = \underline{\beta}^{(2)}\underline{\mathscr{R}}^{s,(2)},\tag{41}$$

where $\underline{\beta}^{(1)}$ and $\underline{\beta}^{(2)}$ are weighting factors. The strain energy associated with the non-uniform deformation is written as

$$\mathcal{W}_{s}(\underline{\mathcal{Y}}) = \mathcal{W}_{s}(\underline{\mathcal{Y}}^{(1)}) + \mathcal{W}_{s}(\underline{\mathcal{Y}}^{(2)}),
= \frac{1}{2} (\underline{\beta} \underline{\mathcal{R}})^{s,(1)} \bullet \underline{\mathcal{R}}^{s,(1)} + \frac{1}{2} (\underline{\beta} \underline{\mathcal{R}})^{s,(2)} \bullet \underline{\mathcal{R}}^{s,(2)}, \tag{42}$$

where \bullet is the state dot product operator. $\mathcal{W}_s(\mathcal{Y}^{(1)})$ in (42) can be expressed as

$$\mathcal{W}_{s}^{(1)} = \int_{\mathcal{X}^{(1)}} \underline{\beta}^{(1)} \underline{\mathcal{R}}_{i}^{s,(1)} \left(\underline{\mathcal{Y}}_{i} - \mathcal{F}_{ij} \underline{\zeta}_{j} \right)^{(1)} d\mathcal{V}',
= \int_{\mathcal{X}^{(1)}} \left\{ \underline{\beta} \underline{\mathcal{R}}_{i}^{s,} \underline{\mathcal{Y}}_{i} \right\}^{(1)} d\mathcal{V}' - \int_{\mathcal{X}^{(1)}} \left\{ \underline{\beta} \underline{\mathcal{R}}_{i}^{s} \mathcal{F}_{ij} \underline{\zeta}_{j} \right\}^{(1)} d\mathcal{V}',
= \int_{\mathcal{X}^{(1)}} \left\{ \underline{\beta} \underline{\mathcal{R}}_{i}^{s} \underline{\mathcal{Y}}_{i} \right\}^{(1)} d\mathcal{V}' - \left(\int_{\mathcal{X}^{(1)}} \underline{\beta} \underline{\mathcal{R}}_{i}^{s} \underline{\zeta}_{j} d\mathcal{V}' \right)^{(1)} \left(\int_{\mathcal{X}^{(1)}} \underline{\omega} \underline{\mathcal{Y}}_{i} \underline{\zeta}_{l} d\mathcal{V}' \right)^{(1)} \mathcal{K}_{lj}^{-1},
= \int_{\mathcal{X}^{(1)}} \left[\underline{\beta} \underline{\mathcal{R}}_{i}^{s} - \left(\int_{\mathcal{X}^{(1)}} \underline{\beta} \underline{\mathcal{R}}_{i}^{s} \underline{\zeta}_{j} d\mathcal{V}' \right) \underline{\omega} \underline{\zeta}_{l} \mathcal{K}_{lj}^{-1} \right]^{(1)} \underline{\mathcal{Y}}_{i}^{(1)} d\mathcal{V}'.$$
(43)

Similarly, we have

$$\mathcal{W}_{s}^{(2)} = \int_{\mathcal{X}^{(2)}} \left[\underline{\beta} \underline{\mathcal{R}}_{i}^{s} - \left(\int_{\mathcal{X}^{(1)}} \underline{\beta} \underline{\mathcal{R}}_{i}^{s} \underline{\zeta}_{j} \, d\mathcal{V}' \right) \underline{\omega} \underline{\zeta}_{i} \mathcal{K}_{lj}^{-1} \right]^{(2)} \underline{\mathcal{Y}}_{i}^{(2)} d\mathcal{V}'. \tag{44}$$

In line with the formulation of the standard correspondence principle the stabilized force state terms at a phreatic material point can be determined as

$$\underline{\mathcal{T}}_{s,i}^{(1)} = \left\{ \underline{\beta} \underline{\mathcal{R}}_{i}^{s} - \left(\int_{\mathcal{X}} \underline{\beta} \underline{\mathcal{R}}_{i}^{s} \underline{\zeta}_{j} \, d\mathcal{V}' \right) \underline{\omega} \underline{\zeta}_{l} \mathcal{K}_{lj}^{-1} \right\}^{(1)}, \tag{45}$$

$$\underline{\mathscr{T}}_{s,i}^{(2)} = \left\{ \underline{\beta} \underline{\mathscr{R}}_{i}^{s} - \left(\int_{\mathscr{X}} \underline{\beta} \underline{\mathscr{R}}_{i}^{s} \underline{\zeta}_{j} \, d\mathscr{V}' \right) \underline{\omega} \underline{\zeta}_{l} \mathscr{K}_{lj}^{-1} \right\}^{(2)}. \tag{46}$$

In this study to simplify (45) and (46) it is assumed that $\beta^{(1)}$ and $\beta^{(2)}$ are constants as

$$\underline{\beta}^{(1)} = \frac{GC^{(1)}}{\omega_0^{(1)}}\underline{\omega},\tag{47}$$

$$\underline{\beta}^{(2)} = \frac{GC^{(2)}}{\omega_0^{(2)}}\underline{\omega},\tag{48}$$

where G is the stabilization parameter, 25,32 C is the micro-elastic modulus, 25 and

$$\omega_0^{(1)} = \int_{\mathscr{X}^{(1)}} \underline{\omega} \, d\mathscr{V}', \tag{49}$$

$$\omega_0^{(2)} = \int_{\mathscr{Y}^{(2)}} \underline{\omega} \, d\mathscr{V}'. \tag{50}$$

It follows that (45) and (46) can be rewritten as

$$\underline{\mathcal{T}}^{s,(1)} = \frac{GC^{(1)}}{\omega_0^{(1)}} \underline{\omega} \underline{\mathcal{R}}^{s,(1)},$$

$$\underline{\mathcal{T}}^{s,(2)} = \frac{GC^{(2)}}{\omega_0^{(2)}} \underline{\omega} \underline{\mathcal{R}}^{s,(2)}.$$
(51)

Then, the effective force state at a phreatic material point can be written as

$$\overline{\underline{\mathcal{T}}} = \underline{\omega} \left\{ \underline{\zeta} \mathcal{K}^{-1} \overline{\sigma} + \frac{GC}{\omega_0} \underline{\mathcal{R}}^s \right\}^{(1)} + \underline{\omega} \left\{ \underline{\zeta} \mathcal{K}^{-1} \overline{\sigma} + \frac{GC}{\omega_0} \underline{\mathcal{R}}^s \right\}^{(2)}.$$
 (52)

The parameters $C^{(1)}$ and $C^{(2)}$ can be determined by the strain energy method assuming an isotropic elastic deformation of the skeleton as follows. For simplicity, a microelastic peridynamic model⁴⁷ is adopted to determine the elastic energy in the solid skeleton.

Let u and u' are the displacement vectors at material points x and x' respectively referring to the current configuration. The rate form of the strain energy density at material point x due to deformation $\eta = u' - u$ can be written as

$$\dot{\mathcal{W}} = \frac{1}{2} \int_{\mathcal{X}^{(1)}} w(\eta, \zeta) \, d\mathcal{V}' + \frac{1}{2} \int_{\mathcal{X}^{(2)}} w(\eta, \zeta) \, d\mathcal{V}',
= \frac{1}{2} \varphi^{(1)} \int_{\mathcal{X}} w(\eta, \zeta) \, d\mathcal{V}' + \frac{1}{2} \varphi^{(2)} \int_{\mathcal{X}} w(\eta, \zeta) \, d\mathcal{V}',$$
(53)

where $\eta = ||\eta||, \zeta = ||\zeta||$, and $\varphi^{(1)}$ and $\varphi^{(2)}$ are defined as follows.

$$\varphi^{(1)} = \frac{\int_{\mathscr{H}^{(1)}} d\mathscr{V}'}{\int_{\mathscr{H}} d\mathscr{V}'},\tag{54}$$

$$\varphi^{(2)} = \frac{\int_{\mathscr{H}^{(2)}} d\mathscr{V}'}{\int_{\mathscr{H}} d\mathscr{V}'}.$$
 (55)

Consider an isotropic deformation of the solid skeleton the stretch of a bond reads

$$\eta = C_1 \zeta, \tag{56}$$

where C₁ is a material constant. The micro-potential²⁵ can be written as

$$w^{(1)} = C^{(1)}C_1^2\zeta/2, (57)$$

$$w^{(2)} = C^{(2)}C_1^2\zeta/2. (58)$$

Substituting (57) and (58) into (53) gives

$$\dot{\mathcal{W}} = \frac{1}{2}\varphi^{(1)} \int_{\mathcal{H}} \frac{1}{2} \left(C^{(1)} \dot{C}_{1}^{2} \zeta \right) d\mathcal{V}' + \frac{1}{2}\varphi^{(2)} \int_{\mathcal{H}} \frac{1}{2} \left(C^{(2)} \dot{C}_{1}^{2} \zeta \right) d\mathcal{V}',
= \frac{1}{2}\varphi^{(1)} \int_{0}^{\delta} \frac{1}{2} \left(C^{(1)} \dot{C}_{1}^{2} \zeta \right) (4\pi\zeta^{2}) d\zeta + \frac{1}{2}\varphi^{(2)} \int_{0}^{\delta} \frac{1}{2} \left(C^{(2)} \dot{C}_{1}^{2} \zeta \right) (4\pi\zeta^{2}) d\zeta,
= \varphi^{(1)} \frac{\pi C^{(1)} \delta^{4}}{4} \dot{C}_{1}^{2} + \varphi^{(2)} \frac{\pi C^{(2)} \delta^{4}}{4} \dot{C}_{1}^{2}.$$
(59)

From the classical elastic theory, the incremental elastic strain energy density of the solid skeleton at a phreatic material point under isotropic deformation reads

$$\dot{\mathcal{W}} = \left\{ \frac{1}{2} \overline{\sigma} : \dot{\epsilon} \right\}^{(1)} + \left\{ \frac{1}{2} \overline{\sigma} : \dot{\epsilon} \right\}^{(2)},
= \left\{ \frac{1}{2} (K \varepsilon_{\nu}) (\dot{\varepsilon}_{\nu}) \right\}^{(1)} + \left\{ \frac{1}{2} (K \varepsilon_{\nu}) (\dot{\varepsilon}_{\nu}) \right\}^{(2)},
= \left\{ \frac{1}{2} K (3 \dot{C}_{1})^{2} \right\}^{(1)} + \left\{ \frac{1}{2} K (3 \dot{C}_{1})^{2} \right\}^{(2)},
= \left\{ \frac{9K}{2} \dot{C}_{1}^{2} \right\}^{(1)} + \left\{ \frac{1}{2} K (3 \dot{C}_{1})^{2} \right\}^{(2)},$$
(60)

where K is the elastic bulk modulus and ε_{ν} is the elastic volumetric strain under isotropic deformation. From (60) and (59) C under three-dimensional condition can be written as

$$C^{(1)} = \varphi^{(1)} \frac{18K}{\pi \delta^4},\tag{61}$$

$$C^{(2)} = \varphi^{(2)} \frac{18K}{\pi \delta^4},\tag{62}$$

Next, we first demonstrate that the fluid flow state in the updated Lagrangian–Eulerian formulation inherits the instability as in the total Lagrangian–Eulerian formulation and then present a stabilization scheme through the energy method for the fluid phase. The two residual fluid flow states at a phreatic material point read

$$\mathcal{R}^{w,(1)} = \underline{\Phi}^{(1)} - \operatorname{grad}(\widetilde{\Phi})^{(1)} \zeta^{(1)}, \tag{63}$$

$$\mathcal{R}^{w,(2)} = \underline{\Phi}^{(2)} - \operatorname{grad}(\widetilde{\Phi})^{(2)} \zeta^{(2)}. \tag{64}$$

Substituting (63) or (64) into the spatial nonlocal pressure gradient (16) generates

$$\operatorname{grad}\left(\underline{\mathscr{R}}^{w}\right) = \left(\int_{\mathscr{X}} \underline{\omega} \, \underline{\Phi} \, \underline{\zeta} \, d\mathscr{V}'\right) \, \mathscr{K}^{-1},$$

$$= \int_{\mathscr{X}} \underline{\omega} \, \underline{\mathscr{R}}^{w} \, \underline{\zeta} \, d\mathscr{V}' \left(\int_{\mathscr{X}} \underline{\omega} \, \underline{\zeta} \otimes \underline{\zeta} \, d\mathscr{V}'\right)^{-1},$$

$$= \int_{\mathscr{X}} \underline{\omega} \, (\underline{\Phi} - \operatorname{grad}(\widetilde{\Phi})\underline{\zeta})\underline{\zeta} \, d\mathscr{V}' \left(\int_{\mathscr{X}} \underline{\omega} \, \underline{\zeta} \otimes \underline{\zeta} \, d\mathscr{V}'\right)^{-1},$$

$$= \left(\int_{\mathscr{X}} \underline{\omega} \, (\underline{\Phi}\underline{\zeta}) \, d\mathscr{V}' - \operatorname{grad}(\widetilde{\Phi}) \int_{\mathscr{X}} \underline{\omega} \, (\underline{\zeta} \otimes \underline{\zeta}) \, d\mathscr{V}'\right) \left(\int_{\mathscr{X}} \underline{\omega} \, \underline{\zeta} \otimes \underline{\zeta} \, d\mathscr{V}'\right)^{-1},$$

$$= \operatorname{grad}(\widetilde{\Phi}) - \operatorname{grad}(\widetilde{\Phi}) \, \mathscr{K} \, \mathscr{K}^{-1} = 0. \tag{65}$$

It is implied by (65) that the correspondence principle for fluid flow in the updated Lagrangian–Eulerian formulation will generate zero-energy mode instability under non-uniform fluid flow conditions. We define the stabilization terms for the fluid flow states at a phreatic material point as

$$\underline{\mathscr{Q}}^{s} = \underline{\lambda}^{(1)} \underline{\mathscr{R}}^{w,(1)} + \underline{\lambda}^{(2)} \underline{\mathscr{R}}^{w,(2)}, \tag{66}$$

where $\underline{\lambda}^{(1)}$ and $\underline{\lambda}^{(2)}$ are positive parameters. The fluid flow dissipation energy in the updated Lagrangian-Eulerian formulation reads

$$\mathcal{W}_{d}^{s} = \frac{1}{2} \left(\underline{\lambda \mathcal{R}}^{w} \right)^{w,(1)} \bullet \underline{\mathcal{R}}^{w,(1)} + \frac{1}{2} \left(\underline{\lambda \mathcal{R}}^{w} \right)^{(2)} \bullet \underline{\mathcal{R}}^{w,(2)}. \tag{67}$$

It follows from (63) and (67) that

$$\mathcal{W}_{d}^{s,(1)} = \int_{\mathcal{X}^{(1)}} \underline{\lambda}^{(1)} \underline{\mathcal{R}}^{w,(1)} \left(\underline{\Phi} - \operatorname{grad}(\widetilde{\Phi})_{i} \underline{\zeta}_{i}\right)^{(1)} d\mathcal{V}',
= \int_{\mathcal{X}^{(1)}} \left\{\underline{\lambda} \underline{\mathcal{R}}^{w} \underline{\Phi}\right\}^{(1)} d\mathcal{V}' - \int_{\mathcal{X}^{(1)}} \left\{\underline{\lambda} \underline{\mathcal{R}}^{w} \operatorname{grad}(\widetilde{\Phi})_{i} \underline{\zeta}_{i}\right\}^{(1)} d\mathcal{V}',
= \int_{\mathcal{X}^{(1)}} \left\{\underline{\lambda} \underline{\mathcal{R}}^{w} \underline{\Phi}\right\}^{(1)} d\mathcal{V}' - \left(\int_{\mathcal{X}^{(1)}} \underline{\lambda} \underline{\mathcal{R}} \underline{\zeta}_{i} d\mathcal{V}'\right)^{(1)} \left(\int_{\mathcal{X}^{(1)}} \underline{\omega} \underline{\Phi} \underline{\zeta}_{j} d\mathcal{V}'\right)^{(1)} \mathcal{K}_{ji}^{-1},
= \int_{\mathcal{X}^{(1)}} \left[\underline{\lambda} \underline{\mathcal{R}}^{w} - \left(\int_{\mathcal{X}^{(1)}} \underline{\lambda} \underline{\mathcal{R}}^{w} \underline{\zeta}_{i} d\mathcal{V}'\right) \underline{\omega} \underline{\zeta}_{j} \mathcal{K}_{ji}^{-1}\right]^{(1)} \underline{\Phi}^{(1)} d\mathcal{V}'.$$
(68)

Similarly, we have

$$\mathcal{W}_{d}^{s,(2)} = \int_{\mathcal{X}^{(1)}} \left[\underline{\lambda \mathcal{R}}^{w} - \left(\int_{\mathcal{X}^{(2)}} \underline{\lambda \mathcal{R}}^{w} \underline{\zeta}_{i} d\mathcal{V}' \right) \underline{\omega \underline{\zeta}}_{j} \mathcal{K}_{ji}^{-1} \right]^{(2)} \underline{\Phi}^{(2)} d\mathcal{V}'. \tag{69}$$

From (15), (68), and (69) the stabilized terms for the fluid flow state accounting for the non-uniform fluid potential state can be written as

$$\underline{\mathscr{Q}}^{s,(1)} = \left\{ \underline{\lambda \mathscr{R}}^{w} - \left(\int_{\mathscr{X}} \underline{\lambda R}^{w} \underline{\zeta}_{i} d\mathscr{V}' \right) \underline{\omega \underline{\zeta}}_{j} \mathscr{K}_{ji}^{-1} \right\}^{(1)}, \tag{70}$$

$$\underline{\mathscr{Q}}^{s,(2)} = \left\{ \underline{\lambda \mathscr{R}}^{w} - \left(\int_{\mathscr{X}} \underline{\lambda R}^{w} \underline{\zeta}_{i} \mathscr{K}_{ji}^{-1} d\mathscr{V}' \right) \underline{\omega \underline{\zeta}}_{j} \right\}^{(2)}. \tag{71}$$

For simplicity, we assume that λ takes the following form

$$\underline{\lambda}^{(1)} = \frac{GK_p^{(1)}}{\omega_0^{(1)}}\underline{\omega},\tag{72}$$

$$\underline{\lambda}^{(2)} = \frac{GK_p^{(2)}}{\omega_0^{(2)}}\underline{\omega},\tag{73}$$

where $K_p^{(1)}$ and $K_p^{(2)}$ are hydraulic micro-conductivities. Then, we obtain

$$\underline{\underline{\mathscr{Q}}}^{s,(1)} = \frac{GK_p^{(1)}}{\omega_0^{(1)}} \underline{\omega} \underline{\mathcal{R}}^{w,(1)},$$

$$\underline{\underline{\mathscr{Q}}}^{s,(2)} = \frac{GK_p^{(2)}}{\omega_0^{(2)}} \underline{\omega} \underline{\mathcal{R}}^{w,(2)}.$$
(74)

Then, the stabilized fluid flow state at material point x is written as

$$\underline{\mathcal{Q}} = \underline{\omega} \left(\mathbf{q} \mathcal{K}^{-1} \underline{\zeta} + \frac{GK_p}{\omega_0} \underline{\mathcal{R}}^{w} \right)^{(1)} + \underline{\omega} \left(\mathbf{q} \mathcal{K}^{-1} \underline{\zeta} + \frac{GK_p}{\omega_0} \underline{\mathcal{R}}^{w} \right)^{(2)}. \tag{75}$$

Next, we derive the material variables through an energy method assuming an isotropic fluid flow. The dissipation potential energy at a phreatic material point reads

$$\mathcal{W}_{d} = \frac{1}{2} \int_{\mathcal{H}^{(1)}} w^{f} (\mathbf{x}', \mathbf{x}) \, d\mathcal{V}' + \frac{1}{2} \int_{\mathcal{H}^{(2)}} w^{f} (\mathbf{x}', \mathbf{x}) \, d\mathcal{V}',$$

$$= \frac{1}{2} \varphi^{(1)} \int_{\mathcal{H}} w^{f} (\mathbf{x}', \mathbf{x}) \, d\mathcal{V}' + \frac{1}{2} \varphi^{(2)} \int_{\mathcal{H}} w^{f} (\mathbf{x}', \mathbf{x}) \, d\mathcal{V}'.$$
(76)

The peridynamic hydraulic micro-conductivity can be related to the classical hydraulic conductivity by equating the peridynamic fluid dissipation potential to the classical fluid dissipation potential at a phreatic material point. For simplicity, we assume a linear pressure field in a porous material body, $p_w = \mathcal{C}_2(\mathbf{1} \cdot \mathbf{x})$ for a three-dimensional case. The fluid flow micro potential²⁵ can be written as

$$w^f = K_p \frac{1}{2} \mathcal{C}_2^2 \zeta. \tag{77}$$

Then we have

$$\mathcal{W}_{d} = \frac{1}{2} \varphi^{(1)} \int_{0}^{\delta} \left(\frac{1}{2} K_{p}^{(1)} \mathcal{C}_{2}^{2} \zeta \right) (4\pi \zeta^{2}) d\zeta + \frac{1}{2} \varphi^{(2)} \int_{0}^{\delta} \left(\frac{1}{2} K_{p}^{(2)} \mathcal{C}_{2}^{2} \zeta \right) (4\pi \zeta^{2}) d\zeta,$$

$$= \varphi^{(1)} \frac{\pi K_{p}^{(1)} \delta^{4}}{4} \mathcal{C}_{2}^{2} + \varphi^{(2)} \frac{\pi K_{p}^{(2)} \delta^{4}}{4} \mathcal{C}_{2}^{2}.$$
(78)

Assuming an isotropic fluid flow, the classical fluid dissipation energy in classical unsaturated poromechanics reads

$$\overline{\mathcal{W}}_{d} = \left\{ \frac{1}{2} (\nabla p_{w}) \frac{k_{r} k_{w}}{\mu} \mathbf{1} (\nabla p_{w}) \right\}^{(1)} + \left\{ \frac{1}{2} (\nabla p_{w}) \frac{k_{r} k_{w}}{\mu} \mathbf{1} (\nabla p_{w}) \right\}^{(2)},$$

$$= \left\{ \frac{3}{2} \frac{k_{r} k_{w}}{\mu} \mathcal{C}_{2}^{2} \right\}^{(1)} + \left\{ \frac{3}{2} \frac{k_{r} k_{w}}{\mu} \mathcal{C}_{2}^{2} \right\}^{(2)}.$$
(79)

where k_w is the intrinsic permeability of saturated porous media and k^r is the relative permeability for the partially saturated case, and μ_w is the water viscosity.

It follows from (78) and (79) that the hydraulic micro-conductivities at a phreatic material point under three-dimensional condition are

$$K_p^{(1)} = \varphi^{(1)} \frac{6k_r k_w}{\mu \pi \delta^4},\tag{80}$$

$$K_p^{(2)} = \varphi^{(2)} \frac{6k_r k_w}{\mu \pi \delta^4}.$$
 (81)

2.4 | Constitutive models and physical laws

We summarize the constitutive models and physical laws. The effective stress tensor can be determined by an isotropic linear elastic model (or a plastic or visco-plastic constitutive model^{33,48-50}) as

$$\dot{\overline{\sigma}} = \mathfrak{C} : \mathfrak{D}^e, \tag{82}$$

where \mathfrak{C} is the forth-order elastic modulus tensor, $^4\dot{\overline{\sigma}}$ is the rotated Cauchy stress, and \mathfrak{D}^e is the elastic deformation rate tensor. Given the velocity gradient tensor the rate of unrotated deformation tensor reads

$$\mathscr{D} = \mathscr{R}^T \left[\frac{1}{2} \left(\mathscr{L} + \mathscr{L}^T \right) \right] \mathscr{R}, \tag{83}$$

where \mathcal{R} is the rotation tensor from the left polar decomposition of \mathcal{F} ,

$$\mathcal{F} = \mathcal{V}\mathcal{R}.\tag{84}$$

Once the effective Cauchy stress tensor is updated it is rotated back to the deformed configuration as follows

$$\dot{\overline{\sigma}} = \mathcal{R}^T \dot{\overline{\sigma}} \mathcal{R}. \tag{85}$$

Similarly, the fluid flux q can be determined by the generalized Darcy's law for unsaturated fluid flow as

$$\mathbf{q} = -\frac{k^r \mathbf{k}_w}{\mu_w} \operatorname{grad}(\widetilde{\Phi}),\tag{86}$$

where $\operatorname{grad}(\widetilde{\Phi})$ is the nonlocal fluid pressure gradient referring to the current configuration and k_w is the intrinsic permeability tensor. For large deformation applications there exists pure rotations that change the reference frame with no deformation. Therefore, the permeability tensor needs to be modified as

$$\mathbf{k}_{w} = \mathbf{\mathcal{R}}^{T} \hat{\mathbf{k}}_{w} \mathbf{\mathcal{R}}. \tag{87}$$

It follows from (87) that (86) 2 can be written as

$$\mathbf{q} = -\mathbf{R} \left[\frac{k^r \mathbf{R}^T \mathbf{k}_w \mathbf{R}}{\mu_w} \operatorname{grad}(\widetilde{\Phi}) \right]. \tag{88}$$

The fluid flow state in the fracture space reads

$$\underline{Q}_{f} = \frac{3}{m_{v}} \underline{\omega} \rho_{w} \mathbf{q}_{f} \underline{\zeta}, \tag{89}$$

where q_f is the fluid flow vector in fracture space. Through Darcy's law for unsaturated fluid flow the fracture fluid flow vector q_f can be written as

$$\mathbf{q}_f = -\frac{k_f^r k_f}{\mu_w} \widetilde{\mathbf{\nabla}} \widetilde{\Phi}_f, \tag{90}$$

where k_f^r is the relative permeability, k_f is the intrinsic permeability of fracture space 24, and $\widetilde{\nabla}\Phi_f$ is the nonlocal fracture fluid pressure gradient determined as

$$\widetilde{\nabla \Phi_f} = \frac{3}{m_v} \int_{\mathscr{X}} \underline{\omega} \, \underline{\Phi_f} \underline{\zeta} \, d\mathscr{V}', \tag{91}$$

-WILEY 15

where

$$\underline{\Phi}_f = p_f' - p_f, \tag{92}$$

and

$$m_{\nu} = \int_{\mathcal{H}} \underline{\omega} \, \underline{\zeta} \, \underline{\zeta} \, \mathrm{d} \mathcal{V}'. \tag{93}$$

The porosity in (3) can be written as²¹

$$\phi = 1 - \frac{(1 - \phi_t)\mathcal{F}}{\mathcal{F}},\tag{94}$$

where ϕ_t is the current configuration porosity and

$$\mathcal{J} = \det(\mathcal{F}). \tag{95}$$

The degree of saturation S_r can be determined from the soil-water retention curve⁵¹⁻⁵⁸ that depends on the volume strain of the solid skeleton (e.g., porosity). In this study, we adopt the one in References 21,59,60 which reads

$$S_r(\mathcal{J}, \phi, p_w) = \left\{ 1 + \left[-a_1 \left(\frac{\mathcal{J}}{1 - \phi} - 1 \right)^{a_2} \mathcal{J} p_w \right]^{a_3} \right\}^{(a_3 - 1)/a_3}, \tag{96}$$

where a_1 , a_2 , and a_3 are all material parameters. Given S_r the relative permeability k^r can be written as

$$k^{r} = S_{r}^{1/2} \left[1 - (1 - S_{r}^{1/m})^{m} \right]^{2}, \tag{97}$$

where $m = (a_3 - 1)/a_3$.

The bond-breakage criterion is based on the deformation energy stored in a poromechanical bond. With the effective force state the energy density in an intact poromechanical bond ζ reads

$$\underline{\dot{\boldsymbol{\varpi}}} = \int_{t}^{t+\Delta t} \left(\underline{\boldsymbol{\mathcal{T}}} - \underline{\boldsymbol{\mathcal{T}}}' \right) \dot{\boldsymbol{\eta}} \, \mathrm{d}t = \int_{t}^{t+\Delta t} \left[\left(\underline{\boldsymbol{\mathcal{T}}} + S_r \underline{\boldsymbol{\mathcal{T}}}_w \right) - \left(\underline{\boldsymbol{\mathcal{T}}}' + S_r' \underline{\boldsymbol{\mathcal{T}}}'_w \right) \right] \dot{\boldsymbol{\eta}} \, \mathrm{d}t, \tag{98}$$

where $\dot{\eta} = \dot{u}' - \dot{u}$ is the relative displacement vector. The bond breakage is realized through the influence function at the material point level for both the solid and fluid phases. The influence function will be replaced by a new influence function $\rho\underline{\omega}$, where ϱ is defined as

$$\underline{\rho} = \begin{cases} 0 & \text{if } \underline{w} \ge \varpi_{cr}, \\ 1 & \text{otherwise.} \end{cases}$$
 (99)

In periporomechanics, the failure at solid skeleton material points is tracked through a scalar damage variable φ .²⁴ This damage variable is defined as the fraction of broken solid bonds at a material point in its horizon

$$\varphi = 1 - \frac{\int_{\mathcal{H}} \varrho \underline{\omega} \, d\mathcal{V}'}{\omega_0},\tag{100}$$

where $\varphi \in [0, 1]$ and ω_0 is defined as

$$\omega_0 = \int_{\mathscr{X}} \underline{\omega} \, d\mathscr{V}'. \tag{101}$$

3 | NUMERICAL IMPLEMENTATION

In this section, we implement the computational large-deformation periporomechanics model through an implicit-implicit fractional step algorithm. With an undrained operator split, the strongly coupled problem is decomposed into an undrained deformation stage and a partially saturated fluid flow stage. The list of neighboring material points of a mixed material point is updated in the deformed configuration at each time step through a dedicated search algorithm. The evolution of phreatic material points across the phreatic line is tracked at each time step through another dedicated search algorithm. In this study, we focus on deformation-driven processes, and loading conditions are applied to the solid skeleton. Thus, we first solve the deformation problem and then the fluid flow process. We note that in other applications, such as hydraulic fracturing wherein fluid pressure drives deformation, it would be preferred to solve the fluid flow first.

3.1 | Time discretization of the deformation stage

In the deformation stage, the equation of motion is solved under undrained condition through an implicit Newton's method.^{24,40}

Given \mathbf{u}_n , $\dot{\mathbf{u}}_n$, $\ddot{\mathbf{u}}_n$ at time step n. Let $\Delta \ddot{\mathbf{u}}_{n+1}^{k+1} = \ddot{\mathbf{u}}_{n+1}^{k+1} - \ddot{\mathbf{u}}_n$ and k is the iteration counter. Following Newmark's method, the displacement, velocity, and acceleration of the solid skeleton at time step n+1 can be written as

$$\ddot{\boldsymbol{u}}_{n+1}^{k+1} = \ddot{\boldsymbol{u}}_{n+1}^{k} + \delta \Delta \ddot{\boldsymbol{u}}_{n+1}^{k+1}, \tag{102}$$

$$\dot{\boldsymbol{u}}_{n+1}^{k+1} = \dot{\boldsymbol{u}}_n + \Delta t \ddot{\boldsymbol{u}}_n + \beta_2 \Delta t \Delta \ddot{\boldsymbol{u}}_{n+1}^{k+1},\tag{103}$$

$$\mathbf{u}_{n+1}^{k+1} = \mathbf{u}_n + \Delta t \dot{\mathbf{u}}_n + \frac{(\Delta t)^2}{2} \ddot{\mathbf{u}}_n + \beta_1 \frac{(\Delta t)^2}{2} \Delta \ddot{\mathbf{u}}_{n+1}^{k+1}, \tag{104}$$

where β_1 and β_2 are numerical integration parameters. For unconditional stability $\beta_1 \geq \beta_2 \geq 0.5$.

The solution procedure for the solid deformation stage with phreatic material points is outlined in Figure 3. A detailed description of its numerical implementation is provided in Algorithm 1. At t_{n+1} , the residual of the motion equation for a mixed material point in the bulk space reads

$$\mathbf{r}^{\mu,k+1} = \rho^{k+1} \ddot{\mathbf{u}}^{k+1} - \int_{\mathcal{H}_n} \underline{\rho}_n \left(\underline{\overline{\mathcal{T}}} - \underline{\overline{\mathcal{T}}}' \right)^{k+1} d\mathcal{V}_n' + \int_{\mathcal{H}_n} \left(S_r \underline{\mathcal{T}}_w - S_r' \underline{\mathcal{T}}_w' \right)^{k+1} d\mathcal{V}_n' - \rho^{k+1} \mathbf{g}.$$
 (105)

Similarly, the residual of the motion equation for a phreatic material point reads

$$\mathbf{r}^{u,k+1} = \rho^{k+1} \ddot{\mathbf{u}}^{k+1} - \int_{\mathcal{H}_n} \underline{\rho}_n \left\{ \left(\underline{\overline{\mathcal{T}}}^{(1)} + \underline{\overline{\mathcal{T}}}^{(2)} \right) - \left(\underline{\overline{\mathcal{T}}}^{\prime(1)} + \underline{\overline{\mathcal{T}}}^{\prime(2)} \right) \right\}^{k+1} d\mathcal{V}_n'$$

$$+ \int_{\mathcal{H}_n} \left\{ S_r \left(\underline{\mathcal{T}}_w^{(1)} + \underline{\mathcal{T}}_w^{(2)} \right) - S_r' \left(\underline{\mathcal{T}}_w^{\prime(1)} + \underline{\mathcal{T}}_w^{\prime(2)} \right) \right\}^{k+1} d\mathcal{V}_n' - \rho^{k+1} \mathbf{g}. \tag{106}$$

The terms of the fluid pressure in (105) are determined from the explicit fluid pressure predictor \tilde{p}_w^{k+1} computed under undrained condition. Given $p_{w,n}$ and $\dot{p}_{w,n}$ at time step n, let $\Delta \dot{\tilde{p}}_{w,n+1} = \dot{\tilde{p}}_{w,n+1} - \dot{p}_{w,n}$. From Newmark's method^{1,25} $\tilde{p}_{w,n+1}$ can be written as

$$\tilde{p}_{w}^{k+1} = p_{w,n} + \Delta t \dot{p}_{w,n} + \beta_3 \Delta t \Delta \dot{\tilde{p}}^{k+1}. \tag{107}$$

Through the undrained operator split, the rate form of $\tilde{p}_{w,n+1}$ at a material point in the bulk reads

$$\dot{\tilde{p}}_{w}^{k+1} = -\left(\phi \frac{S_{r}}{K_{w}} + \phi \frac{\partial S_{r}}{\partial p_{w}}\right)_{n}^{-1} \left[S_{r,n}(\mathcal{L}^{k+1}: \mathbf{1}) + \int_{\mathcal{H}_{n}} \underline{\rho}_{n} \left(\underline{\mathcal{Q}}_{n} - \underline{\mathcal{Q}}_{n}'\right) \, d\mathcal{V}_{n}'\right]. \tag{108}$$

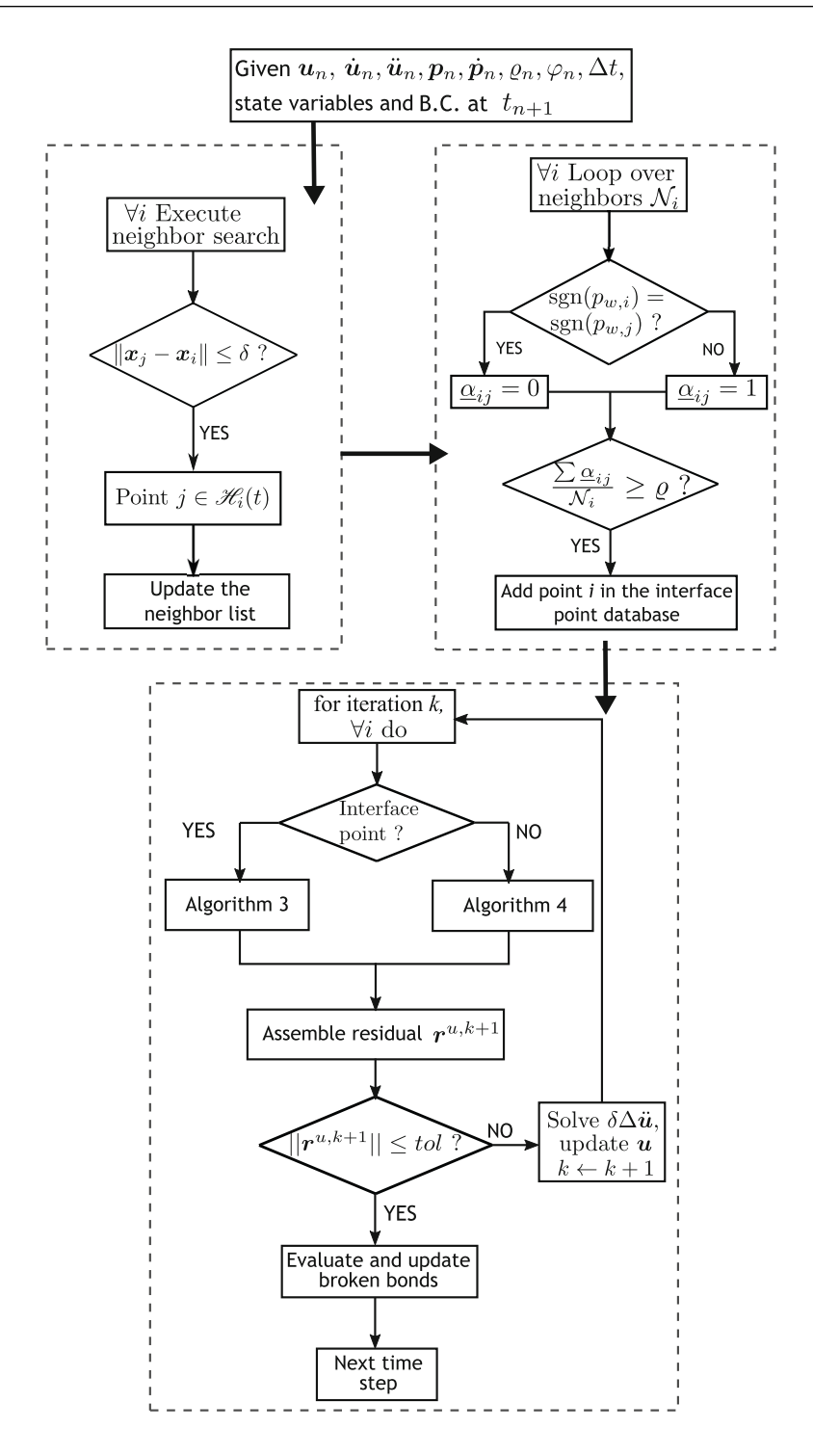


FIGURE 3 Flowchart of Newton's method for solving the motion equation in the deformation stage of the fractional step algorithm for coupled updated Lagrangian–Eulerian periporomechanics.

Similarly, the rate of the predicted fluid pressure at a phreatic material point can be written as

$$\tilde{p}_{w}^{k+1} = -\left(\phi \frac{S_{r}}{K_{w}} + \phi \frac{\partial S_{r}}{\partial p_{w}}\right)_{n}^{-1} \left[S_{r,n}\left(\mathcal{Z}^{(1),k+1} + \mathcal{Z}^{(2),k+1}\right) : \mathbf{1} + \int_{\mathcal{X}_{n}} \underline{\rho}_{n} \left\{\left(\underline{\mathcal{Q}}^{(1)} + \underline{\mathcal{Q}}^{(2)}\right)_{n} - \left(\underline{\mathcal{Q}}^{\prime(1)} + \underline{\mathcal{Q}}^{\prime(2)}\right)_{n}\right\} d\mathcal{V}_{n}'\right].$$
(109)

Algorithms 2 and 3 summarize the algorithms for computing the force states in the residuals of the motion equations at a bulk material point and a phreatic material point, respectively.

Algorithm 1. Fractional step algorithm for the solid deformation stage in fully coupled updated Lagrangian–Eulerian periporomechanics

```
1: procedure GIVEN \boldsymbol{u}_n, \dot{\boldsymbol{u}}_n, \ddot{\boldsymbol{u}}_n, \boldsymbol{p}_{w,n}, \dot{\boldsymbol{p}}_{w,n}, \boldsymbol{p}_{f,n}, \dot{\boldsymbol{p}}_{f,n}, t_n \text{ AND } \Delta t, \text{ SOLVE } \ddot{\boldsymbol{u}}_{n+1} \text{ AND COMPUTE } \overline{\mathcal{V}}_{n+1}
             t_{n+1} = t_n + \Delta t
 2:
             for all points i do
 3:
                   for all points i do
 4.
                          Execute neighbor search \forall i \in \mathcal{B}
 5:
                          if ||x_i - x_i|| \le \delta then
 6:
                                 Add i \in \mathcal{H}_i
 7:
                          end if
 8:
                   end for
 9:
             end for
10:
             Compute the velocity predictor \tilde{\boldsymbol{u}}_{n+1}
11:
             Apply boundary conditions
12:
             Compute the displacement predictor \tilde{\boldsymbol{u}}_{n+1}
13:
             Compute the predictors \widetilde{\boldsymbol{p}}_{w,n+1} and \widetilde{\boldsymbol{p}}_{f,n+1}
14:
             for all points i do
15:
                   for all neighbors i do
16:
                          if sgn(p_{w,i}) = sgn(p_{w,i}) then
17:
18:
                                set \alpha_{ii} = 0
                          else if sgn(p_{w,i})! = sgn(p_{w,j}) then
19:
20:
                                 set \underline{\alpha}_{ii} = 1
                          end if
21:
                   end for
22:
                   if \sum \underline{\alpha}_{ii}/\mathcal{N}_i > \overline{\zeta} then
23:
                          SET i as INTERFACE POINT
24:
                   end if
25:
             end for
26:
             Compute the effective force and fluid force via Algorithm 2
27:
             Compute balance of momentum residual \mathcal{R}_{n+1}^{u,0}
28:
29:
             while ||r_{n+1}^{u,k}|| > \text{tol}_1 \text{ do}
30:
                   Construct tangent operator for the momentum balance \mathcal{A}^{u,k} = \left[ \frac{\partial \mathbf{r}^{u,k}}{\partial \Delta \ddot{\mathbf{u}}^k} \right]_{u,v}
31:
                   Solve the linear system for \delta \Delta \ddot{\boldsymbol{u}}_{n+1}^{k+1}
32:
                   Update \ddot{\boldsymbol{u}}_{n+1}^{k+1}, \boldsymbol{x}_{n+1}^{k+1}, \widetilde{\boldsymbol{p}}_{w,n+1}^{k+1} and \widetilde{\boldsymbol{p}}_{f,n+1}^{k+1}
Check the residual \boldsymbol{\mathcal{R}}_{n+1}^{u,k+1}
33:
34:
                   Set k \leftarrow k+1
35:
             end while
36:
             Update \boldsymbol{p}_{w,n} \leftarrow \widetilde{\boldsymbol{p}}_{w,n+1}, \boldsymbol{p}_{f,n} \leftarrow \widetilde{\boldsymbol{p}}_{f,n+1}
37:
             Evaluate the bond failure criterion and update broken bonds
38:
39: end procedure
```

Substituting (102)–(104) into (105) and using (107), $\Delta \ddot{u}_{n+1}$ can be solved by Newton's method as follows.

$$\mathcal{R}^{u,k+1} = \mathcal{R}^{u,k} + \mathcal{A}^{u,k} \delta \Delta \ddot{\boldsymbol{u}}^{k+1} \approx \mathbf{0}, \tag{110}$$

where \mathcal{R}^u is the global residual vector of the motion equations and \mathcal{A}^u is the global tangent operator of the motion equations

$$\mathcal{A}^{u,k} = \frac{\partial \mathcal{R}^{u,k}}{\partial \Delta \dot{\mathbf{u}}^k}.\tag{111}$$

Algorithm 2. Construct $\overline{\mathcal{T}}_{n+1}$ and $\mathcal{T}_{w,n+1}$ for interface points

```
1: for all interface points i do
              for all neighbors j do
 2:
                     Compute the contribution to \mathcal{X}_{(i)}
 3:
                    if \underline{\alpha}_{ii} = 0 then
 4:
                            Compute the contribution to \mathcal{F}_{i}^{k,(1)}, \mathcal{L}_{i}^{k,(1)}, and \mathcal{D}_{i}^{k,(1)}
  5:
                    end if
  6:
                     if \underline{\alpha}_{ii} = 1 then
  7:
                            Compute the contribution to \mathcal{F}_{i}^{k,(2)}, \mathcal{L}_{i}^{k,(2)}, and \mathcal{D}_{i}^{k,(2)}
                     end if
 9:
              end for
10:
11: end for
      for all interface points i do
12:
              Update the porosity \phi_{:}^{k}
13:
              Compute the volume coupling term \dot{\mathcal{V}}_{i}^{k}
14:
              Compute the rate pressure predictor \dot{\tilde{p}}_{i}^{k}
15:
             \begin{array}{l} \text{Compute } \Delta \boldsymbol{\varepsilon}_i^{k,(1)} \text{ and } \overline{\boldsymbol{\sigma}}_i^{k,(1)} \\ \text{Compute } \Delta \boldsymbol{\varepsilon}_i^{k,(2)} \text{ and } \overline{\boldsymbol{\sigma}}_i^{k,(2)} \end{array}
16:
17:
18: end for
19: for all interface points i do
              for all neighbors j do
20:
                    if \underline{\alpha}_{ii} = 0 then
21:
                            Compute \overline{\underline{\mathcal{F}}}_{ij}^{k,(1)} and \underline{\mathcal{F}}_{w,ij}^{k,(1)}
22:
23:
                    if \underline{\alpha}_{ij} = 1 then
24:
                            Compute \underline{\underline{\mathcal{F}}}_{ij}^{k,(2)} and \underline{\mathcal{F}}_{w,ij}^{k,(2)}
25:
                     end if
26:
              end for
27:
28: end for
```

Solving (111) we obtain

$$\delta \Delta \ddot{\boldsymbol{u}}^{k+1} = -(\mathcal{A}^{u,k})^{-1} \mathcal{R}^{u,k}. \tag{112}$$

Finally, we have

$$\Delta \ddot{\boldsymbol{u}}^{k+1} = \Delta \ddot{\boldsymbol{u}}^k + \delta \Delta \ddot{\boldsymbol{u}}^{k+1}. \tag{113}$$

3.2 | Time discretization of the unsaturated fluid flow stage

Given $p_{w,n}$, $\dot{p}_{w,n}$, and \boldsymbol{u}_n , the unsaturated fluid flow stage solves $\dot{p}_{w,n+1}$ in the updated configuration of the solid skeleton using an implicit Newton's method at time step n+1. Let $\Delta \dot{p}_w^{k+1} = \dot{p}_w^{k+1} - \dot{p}_{w,n}$. From Newmark's method we have

$$\dot{p}_w^{k+1} = \dot{p}_w^k + \delta \Delta \dot{p}_w^{k+1},\tag{114}$$

$$p_w^{k+1} = p_{w,n} + \Delta t \dot{p}_{w,n} + \beta_3 \Delta t \Delta \dot{p}_w^{k+1}. \tag{115}$$

Algorithm 3. Construct $\overline{\mathcal{F}}_{n+1}$ and $\mathcal{F}_{w,n+1}$ for non-interface points

```
1: for all points i do
           for all neighbors i do
 2:
                Compute the contribution to \mathcal{K}_i
 3:
                Compute the contribution to \mathcal{F}_i^k, \mathcal{L}_i^k, and \mathcal{L}_i^k
 4:
           end for
 5:
 6: end for
 7: for all points i do
           Update the porosity \phi_i^k
 8:
           Compute the volume coupling term \hat{\mathcal{V}}_{i}^{k}
 9:
           Compute the rate pressure predictor \hat{p}_{i}^{k}
10:
           Compute \Delta \boldsymbol{\varepsilon}_{i}^{k} and \overline{\boldsymbol{\sigma}}_{i}^{k}
11:
12: end for
13: for all points i do
           for all neighbors j do
14:
                Compute all \underline{\mathcal{F}}_{ij}^k
Compute all \underline{\mathcal{F}}_{wii}^{k}
15:
16:
           end for
17:
18: end for
```

The solution procedure for the unsaturated flow stage with phreatic material points is outlined in Figure 4. A detailed description of its numerical implementation is provided in Algorithm 4. At t_{n+1} , the residual of the mass balance equation for a bulk material point is written as

$$r^{p,k+1} = \left(\phi \frac{S_r}{K_w} + \phi \frac{\partial S_r}{\partial p_w}\right)^{k+1} \dot{p}_w^{k+1} + S_r^{k+1} \mathcal{L} : \mathbf{1} + \int_{\mathcal{X}} \underline{\rho} \left(\underline{\mathcal{Q}} - \underline{\mathcal{Q}}'\right)^{k+1} d\mathcal{V}'. \tag{116}$$

Similarly, the residual of the mass balance equation for a phreatic material point reads

$$r^{p,k+1} = \left(\phi \frac{S_r}{K_w} + \phi \frac{\partial S_r}{\partial p_w}\right)^{k+1} \dot{p}_w^{k+1} + S_r^{k+1} \left(\mathcal{L}^{(1)} + \mathcal{L}^{(2)}\right) : \mathbf{1}$$

$$+ \int_{\mathscr{X}} \underline{\rho} \left\{ \left(\underline{\mathcal{Q}}^{(1)} + \underline{\mathcal{Q}}^{(2)}\right) - \left(\underline{\mathcal{Q}}^{\prime(1)} + \underline{\mathcal{Q}}^{\prime(2)}\right) \right\}^{k+1} d\mathscr{V}'.$$
(117)

Algorithms 5 and 6 show the algorithms for computing the fluid flow and volume rate states for the residual vector of the mass balance equations for the bulk and phreatic material points. Through an implicit Newton's method, $\Delta \dot{p}_{w,n+1}$ can be solved as follows.

$$\mathcal{R}^{p,k+1} = \mathcal{R}^{p,k} + \mathcal{A}^{p,k} \delta \Delta \dot{\mathbf{p}}_w^{k+1} \approx \mathbf{0}, \tag{118}$$

where \mathcal{R}^p is the global residual vector of the mass balance and \mathcal{A}^p is the corresponding global tangent operator

$$\mathcal{A}^{p,k} = \frac{\partial \mathcal{R}^{p,k}}{\partial \Delta \dot{\boldsymbol{p}}_{w}^{k}}.$$
(119)

Solving (118) gives

$$\delta \Delta \dot{\boldsymbol{p}}_{w}^{k+1} = -(\mathcal{A}^{p,k})^{-1} \mathcal{R}^{p,k}. \tag{120}$$

Finally, we have

$$\Delta \dot{\boldsymbol{p}}_{w}^{k+1} = \Delta \dot{\boldsymbol{p}}_{w}^{k} + \delta \Delta \dot{\boldsymbol{p}}_{w}^{k+1}. \tag{121}$$

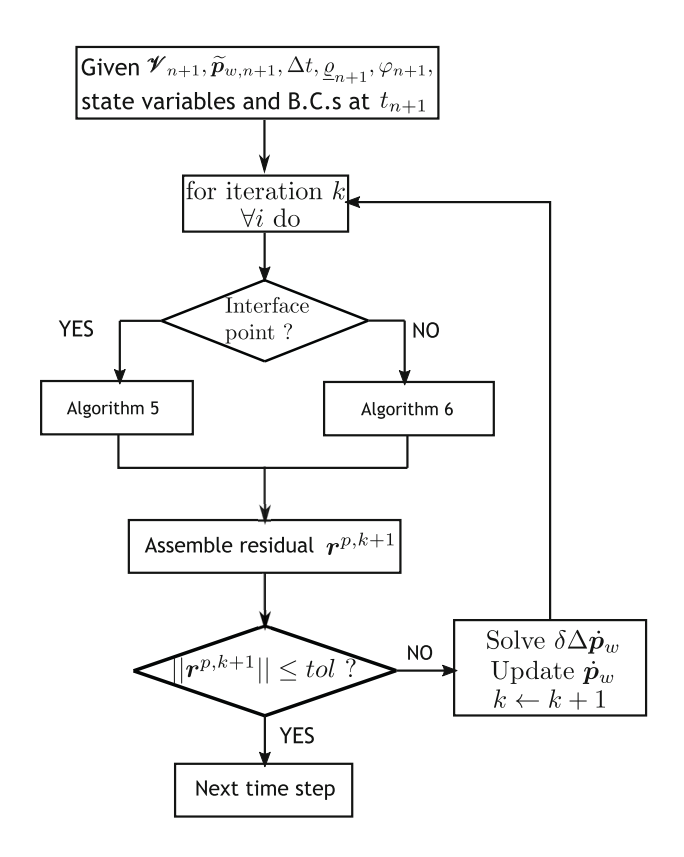


FIGURE 4 Flowchart of Newton's method for solving the mass balance equation in the unsaturated fluid flow stage of the fractional step algorithm for coupled updated Lagrangian–Eulerian periporomechanics.

Algorithm 4. Fractional step algorithm for the partially fluid flow stage in fully coupled updated Lagrangian–Eulerian periporomechanics

```
procedure GIVEN \overline{\mathcal{V}}_{n+1}, \widetilde{\boldsymbol{p}}_{w,n+1}, \widetilde{\boldsymbol{p}}_{w,n+1}, \widetilde{\boldsymbol{p}}_{f,n+1}, \widetilde{\boldsymbol{p}}_{f,n+1}, t_n AND \Delta t, SOLVE \dot{\boldsymbol{p}}_{w,n+1}
                    Compute fluid flow and volume change via Algorithm 5
  2:
                    Compute the balance of mass residual \mathbf{r}_{n+1}^{p,0}
  3:
                    Set k = 0
  4:
                   while ||r^{p,k}|| > \text{tol}_2 \text{ do}
                             Construct tangent \mathcal{A}^{pf,k} = \left[ \left\{ \partial \mathcal{R}^{pf,k} / \partial \Delta \boldsymbol{p}_w^k \right\}; \left\{ \partial \mathcal{R}^{pf,k} / \partial \Delta \boldsymbol{p}_f^k \right\} \right]

Solve \mathcal{A}^{pf,k} \left[ \delta \Delta \boldsymbol{p}_w; \delta \Delta \boldsymbol{p}_f \right]^{k+1} = -\left\{ \mathcal{R}^{p,k}, \mathcal{R}^{f,k} \right\} for \left[ \delta \Delta \boldsymbol{p}_w; \delta \Delta \boldsymbol{p}_f \right]^{k+1}

Update \boldsymbol{p}_w^{k+1} and \boldsymbol{p}_f^{k+1}
  6:
  7:
  8:
                              Check the residual \mathcal{R}^{pf,k+1}
  9:
                              Set k \leftarrow k + 1
10:
                    end while
11:
12:
                    Update \boldsymbol{u}_n \leftarrow \boldsymbol{u}_{n+1}, \boldsymbol{x}_n \leftarrow \boldsymbol{x}_{n+1}
13: end procedure
```

Algorithm 5. Construct Q_{n+1} for interface points

```
1: for all interface points i do
          if p_w < 0 then
 2:
               Compute degree of saturation S_{r,i}^k
 3:
               Compute relative permeability k_i^{r,k}
 4:
          end if
 5:
          if p_w \ge 0 then
 6:
               Set S_{r,i}^k = 1
 7:
               Set k_i^{r,k} = 1
 8:
          end if
 g.
          for all neighbors j do
10:
               if \underline{\alpha}_{ij} = 0 then
11:
                    Compute pressure gradient grad(\tilde{\Phi})_{i}^{k,(1)}
12:
13:
               if \underline{\alpha}_{ii} = 1 then
14:
                    Compute pressure gradient \operatorname{grad}(\tilde{\Phi})_{i}^{k,(2)}
15:
               end if
16:
          end for
17:
          Compute the flux vector \mathbf{q}_{i}^{k,(1)} and \mathbf{q}_{i}^{k,(2)}
18:
19: end for
    for all interface points i do
20:
          for all neighbors j do
21:
               if \underline{\alpha}_{ij} = 0 then
22:
                    Compute \underline{Q}_{ii}^{k,(1)}
23:
               end if
24:
               if \underline{\alpha}_{ij} = 1 then
25:
                    Compute \underline{Q}_{ii}^{k,(2)}
26:
               end if
27:
          end for
28:
29: end for
```

Algorithm 6. Construct Q_{n+1} for non-interface points

```
1: for all points i do
         if p_{w,(i)} < 0 then
 2:
             Compute degree of saturation S_{r,i}^k
 3:
             Compute relative permeability k_i^{r,k}
 4:
         end if
 5:
         if p_{w,i} \ge 0 then
 6:
             Set S_{r,i}^k = 1
 7:
 8:
 9:
         Compute pressure gradient grad(\tilde{\Phi})_{i}^{k}
10:
         Compute the flux vector \mathbf{q}_{i}^{k}
11:
12: end for
    for all points i do
13:
         for all neighbors j do
14:
             Compute fluid flow states \underline{Q}_{ii}^{k}
15:
         end for
16:
17: end for
```

3.3 | Spatial discretization of the updated Lagrangian-Eulerian periporomechanics

The mixed Lagrangian–Eulerian meshfree method is adopted to spatially discretize the coupled governing equations. ²³ Let \mathcal{P} denote the number of total material points in the problem domain and \mathcal{N}_i be the number of material points in the horizon of material point *i*. The spatial discretization of the motion equation and mass balance equation can be written as

$$\mathcal{A}_{i=1}^{P}(\mathcal{M}_{i}\ddot{\boldsymbol{u}}_{i} - \overline{\mathcal{T}}_{i} + \mathcal{T}_{w,i} + \mathcal{F}_{i}) = 0, \tag{122}$$

$$\mathcal{A}_{i-1}^{\mathcal{P}}(S_i + Q_i + \overline{\mathcal{V}}_{s,i} + \mathcal{F}_i) = 0, \tag{123}$$

where

$$\mathcal{M}_i = \left[\rho_s (1 - \phi_i) + \rho_w S_{r,i} \phi_i \right] \mathcal{V}_i \mathbf{1},\tag{124}$$

$$\overline{\mathcal{F}}_{i} = \sum_{j=1}^{\mathcal{N}_{i}} \left[\left(\underline{\overline{\mathcal{F}}}_{ij}^{(1)} + \underline{\overline{\mathcal{F}}}_{ij}^{(2)} \right) - \left(\underline{\overline{\mathcal{F}}}_{ji}^{(1)} + \underline{\overline{\mathcal{F}}}_{ji}^{(2)} \right) \right] \mathcal{V}_{j} \mathcal{V}_{i}, \tag{125}$$

$$\mathcal{F}_{w,i} = \sum_{j=1}^{\mathcal{N}_i} \left[S_{r,i} \left(\underline{\mathcal{F}}_{w,ij}^{(1)} + \underline{\mathcal{F}}_{w,ij}^{(2)} \right) - S_{r,j} \left(\underline{\mathcal{F}}_{w,ji}^{(1)} + \underline{\mathcal{F}}_{w,ji}^{(2)} \right) \right] \mathcal{V}_j \mathcal{V}_i, \tag{126}$$

$$S_i = \phi_i \left(\frac{S_r}{K_w} - \frac{\partial S_{r,i}}{\partial s_i} \right) \dot{p}_{w,i} \mathcal{V}_i, \tag{127}$$

$$Q_{i} = \frac{1}{\rho_{w}} \sum_{i=1}^{N_{i}} \underline{\rho}_{ij} \left[\left(\underline{\mathcal{Q}}_{ij}^{(1)} + \underline{\mathcal{Q}}_{ij}^{(2)} \right) - \left(\underline{\mathcal{Q}}_{ji}^{(1)} + \underline{\mathcal{Q}}_{ji}^{(2)} \right) \right] \mathcal{V}_{j} \mathcal{V}_{i}, \tag{128}$$

$$\overline{\mathcal{V}}_{s,i} = S_{r,i} \left[\mathcal{L}_i^{(1)} + \mathcal{L}_i^{(2)} \right] : \mathbf{1}, \tag{129}$$

 \mathscr{A} is an global assembly operator, ^{23,61} and \mathscr{V}_i and \mathscr{V}_j are the volumes of material points i and j, respectively, in the current configuration. It is noted that (125), (126), (128), and (129) are written in the forms for phreatic material points in which only one term remains for a bulk material point.

In (125) and (126), the effective force state and the water force state are written as

$$\overline{\mathcal{Z}}_{ij}^{(1)} = \left\{ \underline{\omega}_{ij} \underline{\boldsymbol{\zeta}}_{ij} \overline{\boldsymbol{\sigma}}_{i} \right\}^{(1)} \mathcal{K}_{i}^{-1} + \left\{ \underline{\omega}_{ij} \frac{GC}{\omega_{0}} \underline{\mathcal{R}}_{i}^{s} \right\}^{(1)}, \tag{130}$$

$$\overline{\underline{\mathcal{T}}}_{ij}^{(2)} = \left\{ \underline{\omega}_{ij} \underline{\boldsymbol{\zeta}}_{ij} \overline{\boldsymbol{\sigma}}_{i} \right\}^{(2)} \boldsymbol{\mathcal{K}}_{i}^{-1} + \left\{ \underline{\omega}_{ij} \frac{GC}{\omega_{0}} \underline{\boldsymbol{\mathcal{R}}}_{i}^{s} \right\}^{(2)}, \tag{131}$$

$$\underline{\mathscr{T}}_{w,ij}^{(1)} = \left\{ \underline{\omega}_{ij} \underline{\zeta}_{ij} \mathbf{1} p_{w,i} \right\}^{(1)} \mathcal{K}_{i}^{-1}, \tag{132}$$

$$\underline{\mathcal{F}}_{w,ij}^{(2)} = \left\{ \underline{\omega}_{ij} \underline{\zeta}_{ij} \mathbf{1} p_{w,i} \right\}^{(2)} \mathcal{K}_i^{-1}. \tag{133}$$

The fluid flow states and velocity gradients in (128) read

$$\underline{\mathcal{Q}}_{ij}^{(1)} = \left\{ \underline{\omega}_{ij} \rho_{w} \underline{\boldsymbol{\zeta}}_{ij} \boldsymbol{q}_{i} \right\}^{(1)} \boldsymbol{\mathcal{K}}_{i}^{-1} + \left\{ \underline{\omega}_{ij} \frac{GK_{p}}{\omega_{0}} \underline{\mathcal{R}}_{i}^{w} \right\}^{(1)}, \tag{134}$$

$$\underline{\underline{\mathscr{Q}}}_{ij}^{(2)} = \left\{ \underline{\omega}_{ij} \rho_w \underline{\boldsymbol{\zeta}}_{ij} \boldsymbol{q}_i \right\}^{(2)} \boldsymbol{\mathscr{K}}_i^{-1} + \left\{ \underline{\omega}_{ij} \frac{GK_p}{\omega_0} \underline{\mathscr{R}}_i^w \right\}^{(2)}. \tag{135}$$

The velocity gradients in (129) read

$$\mathscr{Z}_{ij,n+1}^{(1)} = \left[\sum_{k=1}^{\mathcal{N}_i} \left(\underline{\omega}_{ij} \underline{\mathscr{Y}}_{ik} \otimes \underline{\zeta}_{ik} \right) \mathscr{V}_k \right]^{(1)} (\mathscr{X}_{ij})^{-1}, \tag{136}$$

$$\mathscr{L}_{ij,n+1}^{(2)} = \left[\sum_{k=1}^{\mathcal{N}_i} \left(\underline{\omega}_{ij} \underline{\mathscr{Y}}_{ik} \otimes \underline{\zeta}_{ik} \right) \mathscr{V}_k \right]^{(2)} (\mathscr{X}_{ij})^{-1}.$$
(137)

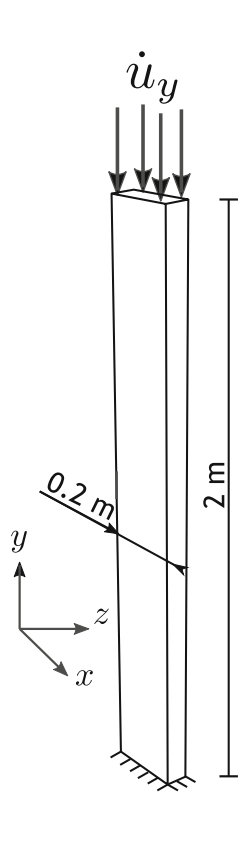
In the next section, we present numerical examples to validate the computational implementation and demonstrate the efficacy of the proposed computational periporomechanics for modeling dynamic failure and fracturing in unsaturated porous media.

4 | NUMERICAL EXAMPLES

4.1 | Example 1: Validation of the coupled stabilization scheme

In this example, we simulate the dynamic consolidation of a three-dimensional unsaturated soil specimen to validate the proposed coupled stabilization scheme. Figure 5 presents the geometry of the soil column, the load, and the boundary conditions. The problem domain is discretized into 9000 uniform mixed material points. The distance of two neighboring material point centers is $\Delta x = 0.1$ m. For the fluid phase, the bottom boundary is prescribed constant fluid pressure, and all other boundaries are impervious. The solid phase is modeled using an isotropic elastic correspondence model. ^{22,23} The intrinsic permeability is assumed isotropic and uniform. The material properties chosen are $\rho_s = 2.1 \times 10^3$ kg/m³, $\rho_w = 1 \times 10^3$ kg/m³, $\mu_w = 1 \times 10^{-3}$ Pa s, initial porosity $\phi_0 = 0.33$, bulk modulus $K = 3.3 \times 10^4$ kPa, shear modulus $\mu_s = 1.62 \times 10^4$ kPa, water bulk modulus $K_w = 2 \times 10^5$ kPa, $K_w = 1 \times 10^{-14}$ m², $K_w = 1 \times 10^{-14}$ m², $K_w = 1 \times 10^{-14}$ m², $K_w = 1 \times 10^{-14}$ m³, $K_w = 1 \times 10^$

Figures 6 and 7 compare the contours of displacement and water pressure, respectively, from the simulations using different values of G. The results of the simulations with the standard correspondence material model (G = 0) show noticeable oscillations. However, the oscillations have disappeared in the results with the stabilized correspondence material model (G = 1.0).



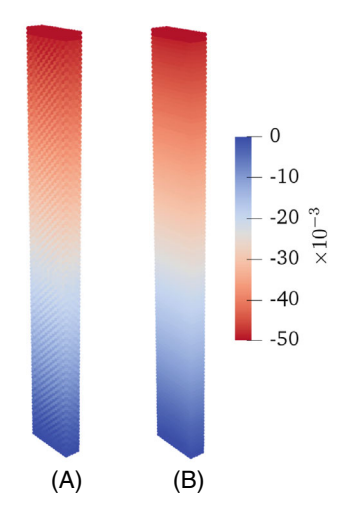


FIGURE 6 Contours of displacement with (A) G = 0.0 and (B) G = 1.0 at $u_v = 0.05$ m.

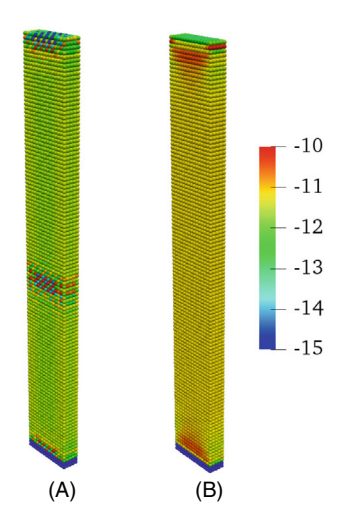


FIGURE 7 Contours of water pressure (kPa) with (A) G = 0.0 and (B) G = 1.0 at $u_v = 0.05$ m.

Figure 8 plots the velocity within the specimen from the simulations with three values of G at $u_y = 0.05$ m on the top boundary. Figure 9 plots the fluid pressure within the specimen with three values of G at the same load step. The results in Figures 8 and 9 show the effect of stabilization could depend on the value of G. This preliminary study implies that the simulation with G = 1.0 removes the oscillations of the velocity and fluid pressure in this example. It is noted that the numerical instability is rooted in the zero-energy mode of deformation associated with the constitutive correspondence principle as elaborated in Section 2.3. The value of G is on the order of 1 in the energy method. ²⁵ In this study, the same value of G is adopted for the solid deformation and unsaturated fluid flow processes.

4.2 | Example 2: Variably saturated flow with an evolving phreatic interface in porous media

In this example, we simulate variably saturated fluid flow with the evolution of a phreatic interface in a rigid porous material. Two cases will be simulated. Case 1 deals with the transient variably saturated fluid flow with no fixed fluid pressure boundary. Case 2 concerns the steady-state variably saturated fluid flow under fixed fluid pressure boundary conditions. We note that the proposed updated Lagrangian–Eulerian periporomechanics is a strong nonlocal formulation in which the zero fluid pressure along the phreatic interface is imposed. Indeed, in this strong nonlocal framework saturated or

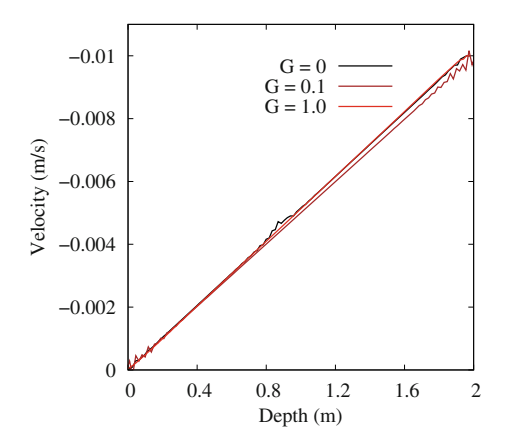


FIGURE 8 Variation of velocity with depth at $u_v = 0.05$ m from the simulations with three values of G.

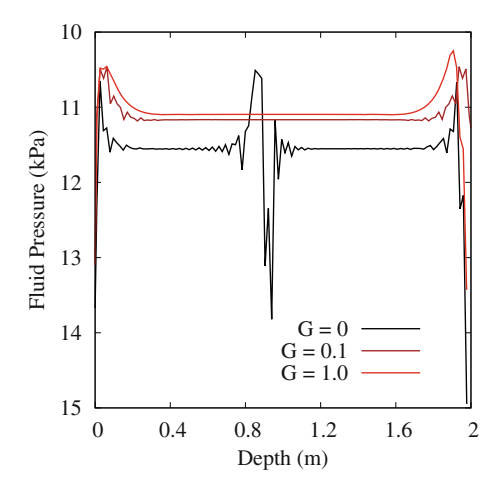


FIGURE 9 Variation of water pressure with depth at $u_v = 0.05$ m from the simulations with three values of G.

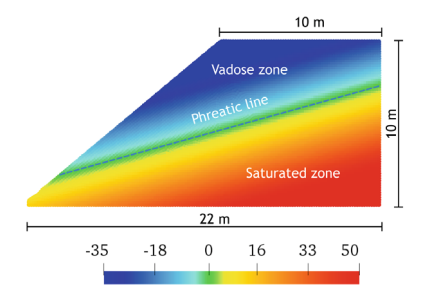


FIGURE 10 Problem setup for Example 2 and the contour of initial fluid pressure (kPa) with a phreatic line for case 1.

unsaturated fluid flow between material points is driven by the fluid potential difference between them. First, we present the results of case 1. Figure 10 plots the problem setup and the contour of the initial fluid pressure with a phreatic line. The initial fluid pressure is prescribed through a linear function of the distance above and below the initial phreatic line as shown in Figure 10. The solid skeleton is assumed rigid. All fluid boundaries are impervious. The problem domain is discretized into 15,000 uniform mixed material points with $\Delta x = 0.15$ m. The initial phreatic line is determined through the search Algorithm 2 introduced in Section 3. The material properties chosen are $\rho_w = 1 \times 10^3$ kg/m³, $\mu_w = 1 \times 10^{-3}$ Pa s, $K_w = 2 \times 10^5$ kPa, $k_w = 1 \times 10^{-15}$ m², $a_1 = 0.038$, $a_2 = 3.49$, $a_3 = 3.0$, $a_3 = 3.0$, $a_4 = 3.0$ kPa. The horizon is $a_4 = 3.0$ total simulation time $a_4 = 3.0$ h (hour) with $a_4 = 3.0$

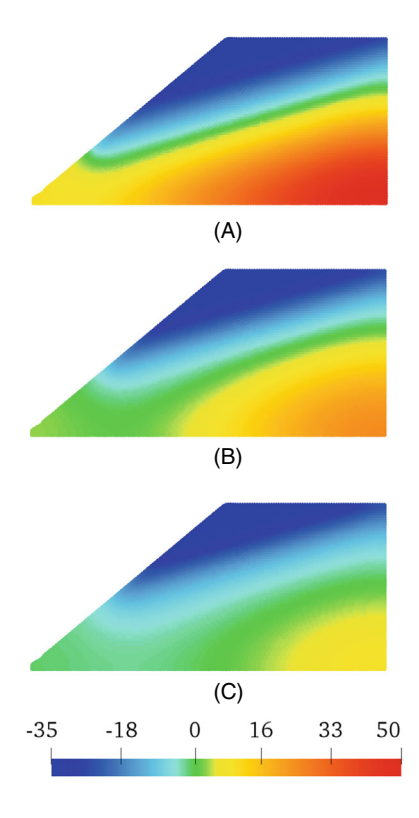


FIGURE 11 Contours of the water pressure (kPa) in the problem domain at (A) t = 1 h, (B) t = 4 h, and (C) t = 8 h for case 1.

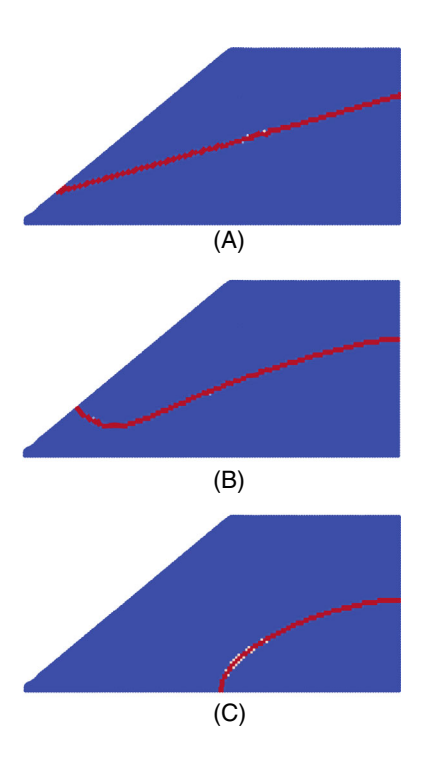


FIGURE 12 Evolution of the phreatic interface (red line) in the problem domain at (A) t = 1 h, (B) t = 4 h, and (C) t = 8 h for case 1.

Figures 11 and 12 plot the results of the simulation at (a) t = 1 h, (b) t = 4 h, and (c) t = 8 h. Fluid flow in the problem domain is driven by the initial state of the fluid pressure. The initial spatial variation of fluid pressure drives fluid flow toward the unsaturated zone causing the phreatic interface to move toward the right bottom of the problem domain. The initial straight phreatic line becomes curved because of the saturated and unsaturated fluid flow within the problem domain.

Next, we present the results of case 2. In this case, we simulate the steady-state phreatic interface in the rigid porous material given the fixed fluid pressure boundaries as shown in Figure 13. We refer to the literature⁶² for modeling free boundary seepage in porous media through the FEM. We note that the steady state phreatic interface is simulated by the unsaturated fluid flow model in this study, which is different from the solution for free-boundary seepage through a saturated fluid flow model in Reference 62. As shown in Figure 13, an initial fluid pressure with a postulated phreatic line in the problem domain is prescribed through the method for case 1 to reduce the overall simulation time. The material parameters and spatial discretization are the same as adopted for case 1. The total simulation time t = 40 h with $\Delta t = 10$ s. The results are presented in Figures 14-16.

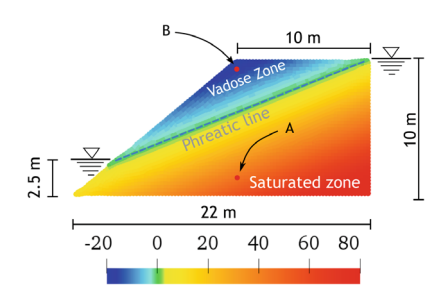


FIGURE 13 Initial phreatic line and fluid boundary conditions for case 2.

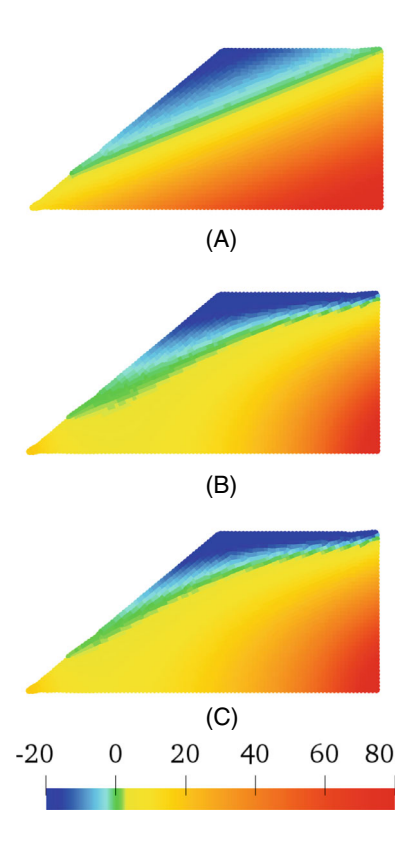


FIGURE 14 Contours of the water pressure (kPa) in the problem domain at (A) t = 0 h, (B) t = 8 h, and (C) t = 40 h for case 2.

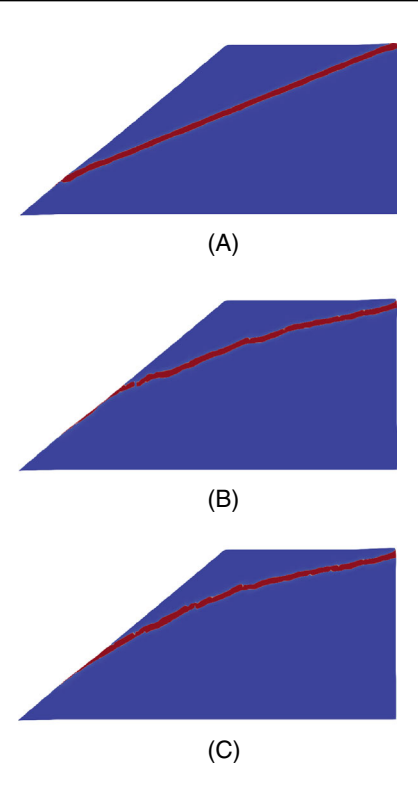
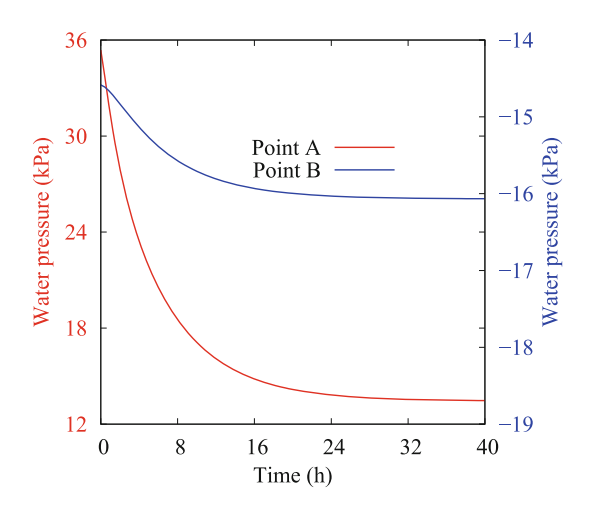


FIGURE 15 Evolution of the phreatic interface (red line) in the problem domain at (A) t = 0 h, (B) t = 8 h, and (C) t = 40 h for case 2.



 $FIGURE\ 16 \quad \mbox{Variation of water pressure with time at two points in the saturated zone and vadose zone respectively for case 2.}$

Figure 14 presents the contours of water pressure at different loading stages. Figure 15 plots the evolution of phreatic interface in the problem domain. Figure 16 plots the variation of water pressure at the two points in the saturated zone and vadose zone respectively as shown in Figure 16. The results in Figure 16 show that the water pressures at both points have reached a steady state. Thus, we can conclude that the phreatic interface shown in Figure 15C is the steady state under the fixed fluid pressure boundary conditions in Figure 13. It is noted that the shape of the steady-state phreatic interface Figure 15C is qualitatively consistent with the results reported in Reference 9.

In summary, this example demonstrates that the implemented variably saturated periporomechanics with a dedicated search algorithm for phreatic material points can adequately model the evolution of the phreatic interface under partially saturated fluid flow condition in porous media.

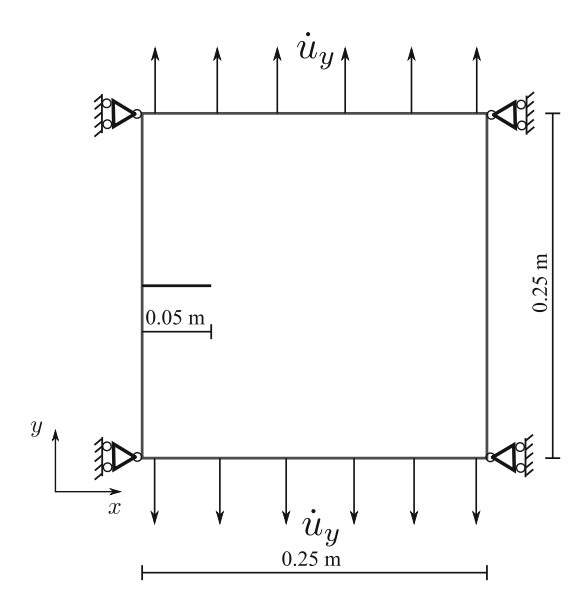
4.3 | Example 3: Mode I cracking

In this example, we simulate mode I crack propagation and unsaturated fluid flow in a porous body in two dimensions to validate the updated Lagrangian–Eulerian fracturing periporomechanics framework. It is worth noting that the mode I cracking in this example can be relevant to desiccation cracking in unsaturated porous media (e.g., unsaturated clay). We compare the numerical results from the updated Lagrangian formulation in this study to the results from the total Lagrangian periporomechanics in Reference 24. We note that the results in Reference 24 were validated against the XFEM results in Reference 19. Figure 17 presents the problem geometry, the boundary conditions, and the load. The pre-existing crack is defined by eliminating interaction between material points across the crack plane. All fluid phase boundaries of the specimen are assumed impermeable. The problem domain is discretized into 20,000 uniform mixed material points with $\Delta x = 0.0025$ m.

The solid phase is modeled using an isotropic elastic correspondence constitutive model. ^{22,23} The material properties are $\rho_s = 2 \times 10^3$ kg/m³, $\rho_w = 1 \times 10^3$ kg/m³, $\mu_w = 1 \times 10^{-3}$ Pa s, initial porosity $\phi_0 = 0.25$, $G_0 = 225$ J/m², $K = 1.346 \times 10^7$ kPa, $\mu_s = 1.095 \times 10^7$ kPa, intrinsic permeability $k_w = 1 \times 10^{-16}$ m², $a_1 = 0.038$, $a_2 = 3.49$, $a_3 = 1.78$, and $a_3 = 1.2 \times 10^4$ kPa. The horizon $\delta = 3.05$ Δx . The stabilization parameter G = 1.0. The initial uniform effective stress $\overline{\sigma} = -13$ kPa. The initial water pressure in the specimen is -15 kPa ($S_r = 0.87$). The loading rate $u_y = 2.0 \times 10^{-6}$ m/s. The total loading time t = 1000 s with $\Delta t = 0.5$ s.

The results are presented in Figures 18-20. Figure 18 compares the reaction force versus the applied displacement on the top boundary from the simulations using the updated Lagrangian formulation to the results from the total Lagrangian formulation. The results in Figure 18 show good agreement between the two curves before the peak load. The slight difference between the two curves after the peak load could be due to the fact that the neighboring points of a mixed material point are updated on each time step in the updated Lagrangian formulation.

Figures 19 and 20 plot the contours of damage variable and water pressure at $u_y = 0.002$ m respectively from the simulations using total and updated Lagrangian formulations. The results in both figures show that the crack opening leads to a similar development of negative pressures (larger matric suction) in the vicinity of the crack. The negative water pressures are due to the fluid flow into the crack space in the mode I cracking process. The results from the total and updated Lagrangian formulations are in good agreement, while there is a slight difference in both the value of water pressure and the length of crack propagation. We note that the mode I crack propagation in this example is brittle in nature. Thus, it is postulated that large deformation is not required for the crack to propagate. Indeed, this postulation is supported by the consistency between the results from the updated and total Lagrangian formulations.



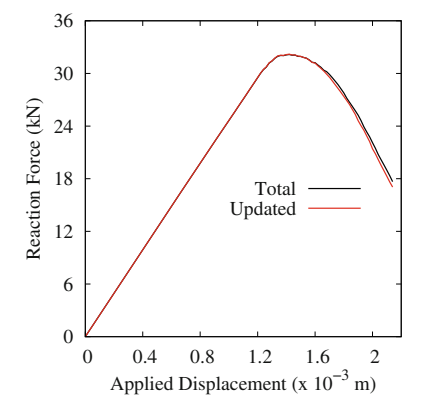


FIGURE 18 Comparison of the loading curves from the total and updated Lagrangian formulations.

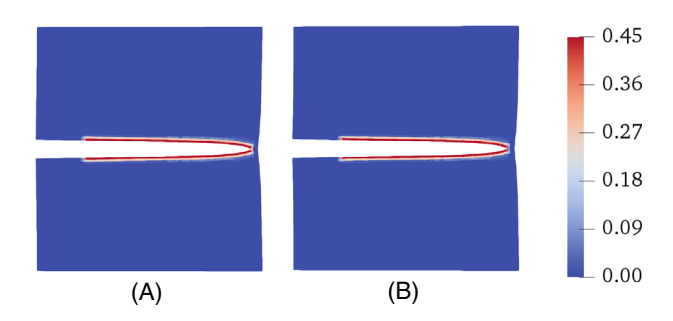


FIGURE 19 Contours of damage variable (φ) from the simulations using (A) total and (B) updated Lagrangian formulations at $u_y = 0.002 \text{ m}$ (×50).

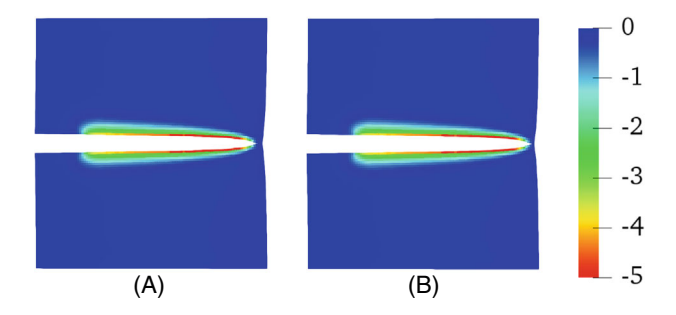


FIGURE 20 Contours of water pressure (MPa) from the simulations using (A) total and (B) updated Lagrangian formulations at $u_y = 0.002 \text{ m} (\times 50)$.

4.4 Wetting collapse of an unsupported vertical cut

In this example, we simulate the wetting collapse of an unsupported vertical cut in an unsaturated soil. Figure 21 depicts the problem domain and boundary conditions. The problem domain is discretized into 13,000 mixed material points with $\Delta x = 0.1$ m.

The solid skeleton is modeled using a critical state elastoplastic constitutive model for unsaturated porous media in Reference 23. The material parameters are $\rho_s = 2.3 \times 10^3$ kg/m³, $\rho_w = 1 \times 10^3$ kg/m³, $\mu_w = 1 \times 10^{-3}$ Pa s, $\phi_0 = 0.25$, $K = 5.56 \times 10^4$ kPa, $\mu_s = 1.064 \times 10^4$ kPa, $K_w = 2 \times 10^5$ kPa, $k_w = 1 \times 10^{-8}$ m/s, $a_1 = 0.038$, $a_2 = 3.49$, $a_3 = 1.78$, $a_3 = 2.5$ kPa. For the plastic model, initial pre-consolidation pressure $\overline{p}_{c0} = -500$ kPa, specific volume at unit pre-consolidation pressure N = 2.2, critical state line slope M = 1, swelling index $\kappa = 0.03$, compression index $\lambda = 0.13$, and fitting parameters $b_1 = 0.185$ and $b_2 = 1.42$. The horizon $\delta = 3.05\Delta x$. The stabilization parameter G = 0.1. The initial water pressure $p_w = -50$ kPa

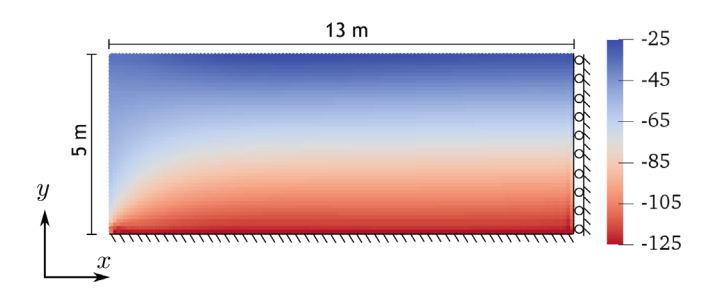


FIGURE 21 Problem setup for Example 4 and the contour of the initial effective stress in y-direction (kPa).

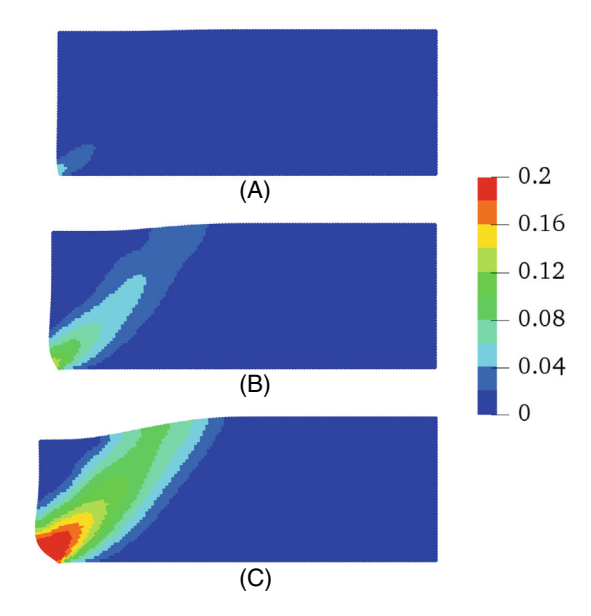


FIGURE 22 Contours of plastic shear strain at (A) $p_w = -23.3$ kPa, (B) $p_w = -21.9$ kPa, and (C) $p_w = -20.5$ kPa ($\times 2$).

(i.e., matric suction = 50 kPa) throughout the problem domain. The vertical effective stress is prescribed by the equation $-\sigma_y = \rho_s gh + S_r p_{w,0}$, where h is the depth from the top surface. The horizontal effective stress $\overline{\sigma}_x = S_r p_{w,0}$. In this example, the wetting collapse of the soil is simulated by uniformly reducing the matric suction in the problem domain.

Figures 22 and 23 plot the contours of plastic shear and plastic volume strains, respectively, at three load steps of (a) $p_w = -23.3$ kPa, (b) $p_w = -21.9$ kPa, and (c) $p_w = -20.5$ kPa. Here the plastic shear strain ε_s^p is the equivalent plastic strain, that is, $\varepsilon_s^p = \sqrt{\frac{2}{3}} \| \varepsilon^p - \frac{1}{3} \text{tr}(\varepsilon^p) \mathbf{1} \|$. The results in Figure 22 reveal that the failure is initiated at the left-bottom corner of the vertical cut from where the deformation band propagates upward. Figure 23 shows that the maximum dilatation appears to occur at the free upper surface of the soil. As the soil deforms outward, this zone of dilatation propagates downward along with the shear band as shown in Figures 22 and 23B,C. It is noted that the second-order work criterion^{23,64,65} is useful to detect failure zones including shear bands in porous media. Thus, in this example we validate our results through the second-order work criterion. The second-order work $d\mathcal{W}$ in unsaturated porous media through the effective stress concept⁶⁵ can be written as

$$dW = d\overline{\sigma} : d\varepsilon. \tag{138}$$

Figure 24 presents the contours of the second-order work in the problem domain at three loading stages. The results in Figures 24 and 22 demonstrate that the zone of negative second-order work is consistent with the localized shear zone in the problem domain.

Next, we repeat the same simulation with a finer spatial discretization with 26,000 material points. The same constant horizon (i.e., 0.305 m) is utilized for both analyses. The results of the two simulations are compared in Figures 25 and 26.

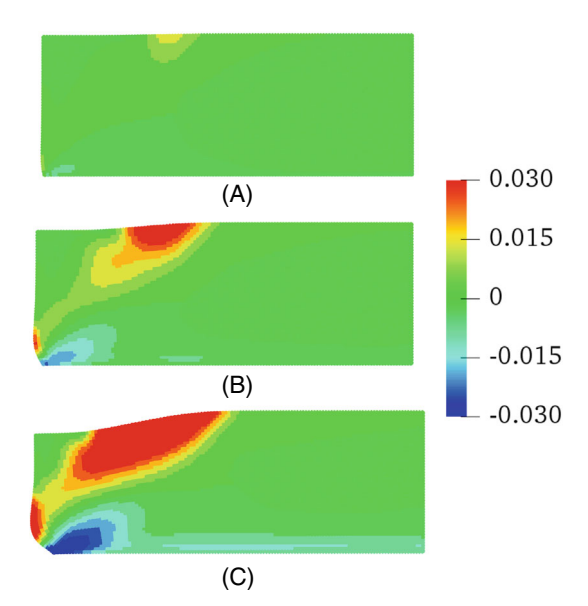


FIGURE 23 Contours of plastic volume strain at (A) $p_w = -23.3$ kPa, (B) $p_w = -21.9$ kPa, and (C) $p_w = -20.5$ kPa (×2).

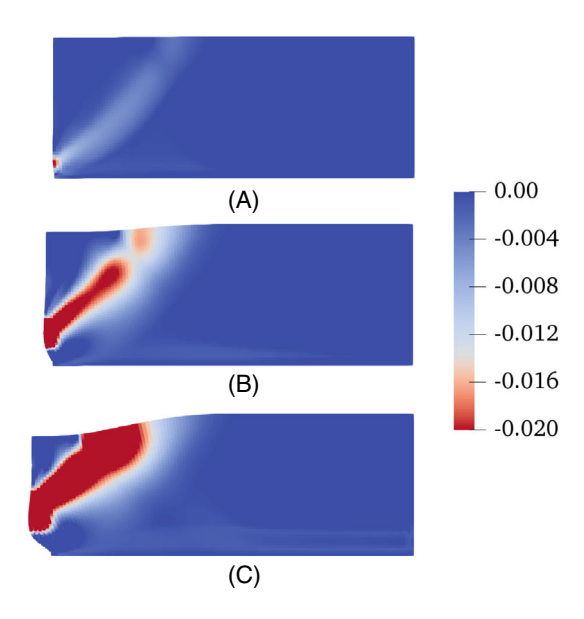


FIGURE 24 Contours of second-order work at (A) $p_w = -23.3$ kPa, (B) $p_w = -21.9$ kPa, and (C) $p_w = -20.5$ kPa (×2).

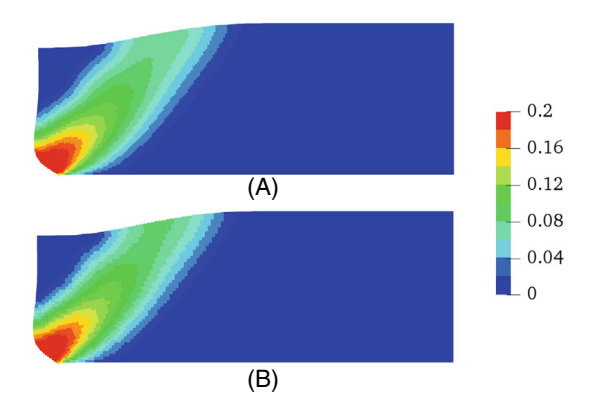


FIGURE 25 Contours of plastic shear strain from the simulations with (A) 26,000 material points and (B) 13,000 material points (×2).

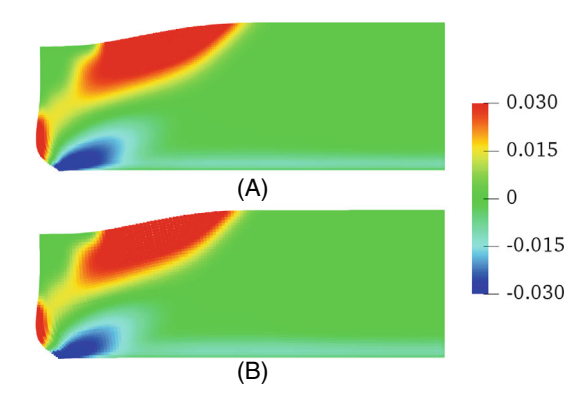


FIGURE 26 Contours of plastic volume strain from the simulations with (A) 26,000 material points and (B) 13,000 material points (×2).

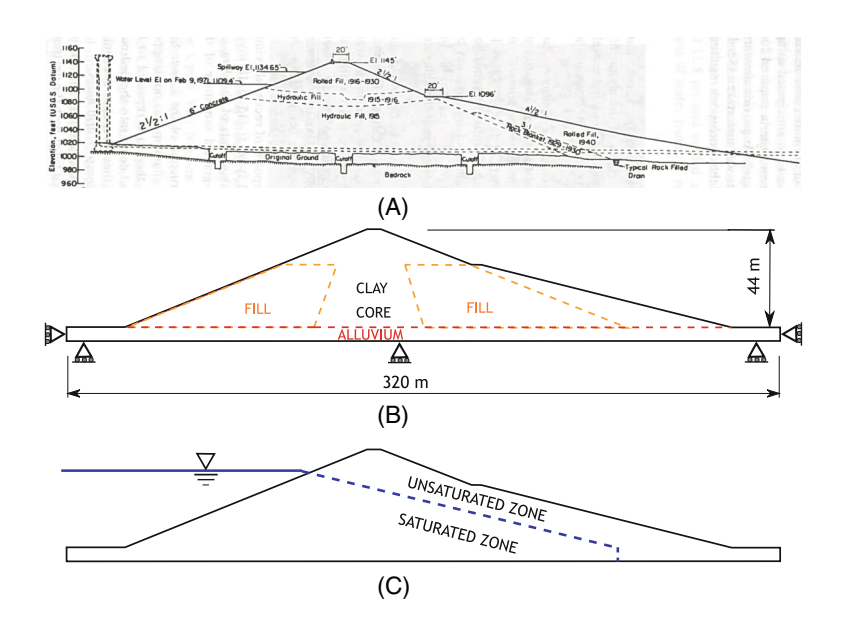


FIGURE 27 (A) Schematic of the dimensions of the dam reported in the literature, (B) Geometry, soil layers within the dam and boundary conditions in this study, and (C) Sketch of the water table in the reservoir and the phreatic line in the dam.

Figure 25 plots the contour of plastic shear strain at the same load step. Figure 26 presents the contour of plastic volume strain at the same load step. The results demonstrate that the contours of shear and volume strains from both simulations are in good agreement. The width of the deformation zone and magnitude of the plastic deformation appear insensitive to the two spatial discretizations. It may be due to the same horizon adopted for the two simulations. We note that the proposed large-deformation periporomechanics framework can capture the Roscoe, Arthur, and Coulomb angles with an appropriate constitutive model (e.g., a non-associative plastic model with Drucker–Prager yield criterion) as shown in the literature, ^{66,67} which is beyond the scope of the present work.

4.5 Dynamic failure of a dam triggered by earthquake

In this example, we demonstrate the efficacy of the proposed computational periporomechanics for modeling the dynamic failure of variably saturated porous media under earthquake loading. For this purpose, we simulate the dynamic failure of the Lower San Fernando Dam during the 1971 San Fernando earthquake ($M_w = 6.6$). We refer to the celebrated literature^{12,68,69} for more information about the post-earthquake investigation of this event. Figure 27 shows (a) the sketch of the geometry of the dam reported in the literature, ⁶⁹ (b) the geometry and boundary conditions adopted in this study, and (c) the water table in the reservoir and the phreatic line within the dam. The base of the dam is constrained against the

The bulk of the dam is made of various types of fines. 12 The core material is simplified as a single slightly overconsolidated clay in this example. The remainder of the dam is composed of a looser and weaker hydraulic filler material outlined in brown in Figure 27 . The input parameters for both materials are $\rho_s = 2 \times 10^3$ kg/m³, $\rho_w = 1 \times 10^3$ kPa, $\rho_w = 1 \times 10^3$ kPa. The plastic material parameters are $\rho_c = 1 \times 10^3$ kPa, $\rho_w = 1 \times 10^3$ kPa, $\rho_w = 1 \times 10^3$ kPa. The plastic material parameters are $\rho_c = 1 \times 10^3$ kPa, $\rho_w = 1 \times 10^3$ kPa, $\rho_w = 1 \times 10^3$ kPa. The plastic material the parameters are $\rho_c = 1 \times 10^3$ kPa, $\rho_w = 1 \times 10^3$ kPa, ρ

Figure 28A,B plots the initial geostatic stress and initial water pressure within the dam, which are generated by a quasi-static elastic analysis. With the crest of the dam taken as the datum, the initial effective stress is computed by the gravitational load on the soil within the dam. Pore water pressure along the upstream slope of the dam is prescribed by $p_w = \rho_w gh$, where h is the distance between the water table and the upstream slope. Pore water pressure and matric suction within the dam are computed through the seepage analysis as in Reference 1. The negative water pressure in the vadose zone is prescribed by $p_w = -\rho_w gh$, where h is the vertical distance above the phreatic line.

Figure 29 plots the acceleration profile recorded during the earthquake. The strong ground motion only lasted for 12 s. The acceleration profile in the blue frame marks the input data in this study. In the coupled analysis, this acceleration profile is applied to the bottom of the dam as shown in Figure 27. The results are presented in Figures 30 and 31.

Figure 30 plots the snapshots of the equivalent plastic shear strain within the dam at (a) t = 4 s, (b) t = 10 s, and (c) t = 16 s respectively. The results show that the large plastic shear strain has occurred at the toe of the upstream slope and the location beneath the core of the dam. The results may imply that failure initiated at the toe and progressed toward the core of the dam. Figure 31 presents the contours of water pressure within the dam at the same three time steps. The results in Figure 31 show that the water pressure increased at the base of the dam, which may imply the liquefaction of the soil under the dam core during the earthquake. The numerical results are consistent with the results based on the mixed FEM in Reference 1. For a more realistic simulation of the dynamic failure of the dam under earthquake loads, a more representative constitutive model for different zones of soils within the dam will be required, which is beyond the scope of the present work.

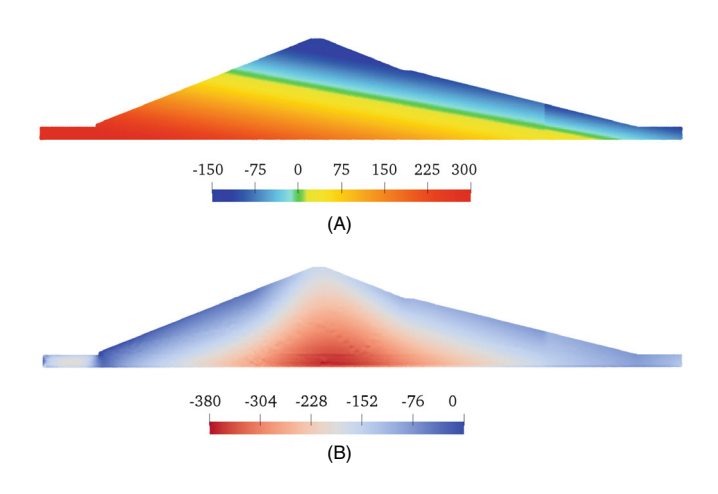


FIGURE 28 Contours of (A) the initial water pressure (kPa), and (B) the initial vertical effective stress (kPa) in the numerical model.

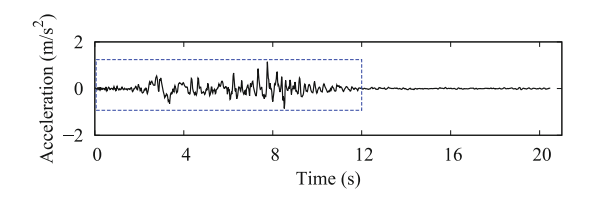


FIGURE 29 Recorded acceleration profile during the earthquake (Pacoima Dam accelerogram, http://www.strongmotioncenter.org).

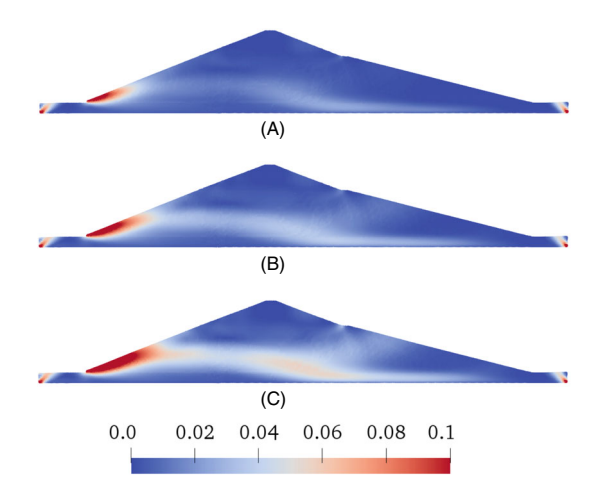


FIGURE 30 Snapshots of the contours of the plastic shear strain within the dam at (A) t = 4 s, (B) t = 10 s, and (C) t = 16 s.

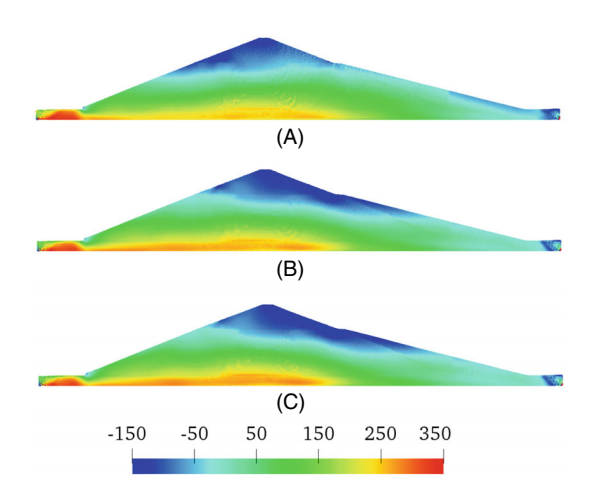


FIGURE 31 Snapshots of the contours of the water pressure (kPa) within the dam at (A) t = 4 s, (B) t = 10 s, and (C) t = 16 s.

5 | CLOSURE

In this study, we have formulated a computational coupled large-deformation periporomechanics paradigm assuming passive air pressure for modeling dynamic failure and fracturing in variably saturated porous media. In this new computational periporomechanics paradigm, the coupled governing equations for both bulk and fracture material points are formulated in the current configuration through the updated Lagrangian–Eulerian framework. It is hypothesized that the horizon of a mixed material point remains spherical, and its neighbor points are determined in the current configuration. As a significant novelty, the mixed phreatic material points across the phreatic line are explicitly considered through the mixed peridynamic state concept. To incorporate the classical constitutive models into the nonlocal framework, we have developed the coupled constitutive correspondence principle with stabilization in the updated Lagrangian–Eulerian framework for both bulk and phreatic material points. We have numerically implemented the coupled large-deformation periporomechanics paradigm through an implicit-implicit fractional-step algorithm in time and a hybrid updated Lagrangian–Eulerian meshfree method in space. We first present numerical examples to validate the implemented coupled stabilization scheme and the fluid flow across the phreatic line in partially saturated porous media. We then conduct numerical examples to demonstrate the robustness and efficacy of the proposed computational framework in modeling fracturing and failure in partially saturated deformable porous media under static and dynamic loads.

ACKNOWLEDGMENTS

This work has been supported by the US National Science Foundation under contract numbers 1659932 and 1944009. The support is gratefully acknowledged. We thank the two anonymous reviewers for their expert reviews of this article.

DATA AVAILABILITY STATEMENT

The data that support the findings of this study are available from the corresponding author upon reasonable request.

ORCID

Xiaoyu Song https://orcid.org/0000-0003-0409-3761

REFERENCES

- 1. Zienkiewicz OC, Chan A, Pastor M, Schrefler B, Shiomi T. Computational Geomechanics. Vol 613. Citeseer; 1999.
- 2. Lewis RW, Schrefler B. The Finite Element Method in the Static and Dynamic Deformation and Consolidation of Porous Media. John Wiley & Sons; 1998.
- 3. Simo JC, Hughes TJ. Computational Inelasticity. Vol 7. Springer Science & Business Media; 1998.
- 4. Holzapfel G. Nonlinear Solid Mechanics. A Continuum Approach for Engineering. John Wiley & Sons; 2001.
- 5. De Borst R, Crisfield MA, Remmers JJ, Verhoosel CV. Nonlinear Finite Element Analysis of Solids and Structures. John Wiley & Sons; 2012.
- 6. Borja RI. Plasticity. Vol 2. Springer; 2013.
- 7. Fung YC. Biomechanics: Mechanical Properties of Living Tissues. Springer Science & Business Media; 2013.
- 8. Terzaghi K, Peck RB. Soil Mechanics. Engineering Practice. John Wiley and Sons, Inc; 1948.
- 9. Fredlund DG, Rahardjo H, Fredlund MD. Unsaturated Soil Mechanics in Engineering Practice. John Wiley & Sons; 2012.
- 10. Lu N, Mitchell JK. Geotechnical Fundamentals for Addressing New World Challenges. Springer; 2019.
- 11. Cowin SC, Doty SB. Tissue Mechanics. Springer; 2007.
- 12. Seed HB, Lee KL, Idriss IM, Makdisi FI. The slides in the San Fernando dams during the earthquake of February 9, 1971. *J Geotechn Eng Div.* 1975;101(7):651-688.
- 13. Bray JD, Seed RB, Cluff LS, Seed HB. Earthquake fault rupture propagation through soil. J Geotech Eng. 1994;120(3):543-561.
- 14. Kramer SL. Geotechnical Earthquake Engineering. Pearson Education India; 1996.
- 15. Bray JD, Rodriguez-Marek A. Characterization of forward-directivity ground motions in the near-fault region. *Soil Dyn Earthq Eng.* 2004;24(11):815-828.
- 16. Matasovic N, Kavazanjian Jr E, Augello AJ, Bray JD, Seed RB. Solid waste landfill damage caused by 17 January 1994 Northridge earthquake; Vol. 17, 1994:221-229; The Northridge, California, Earthquake.
- 17. Bray JD, Travasarou T. Simplified procedure for estimating earthquake-induced deviatoric slope displacements. *J Geotechn Geoenviron Eng.* 2007;133(4):381-392.
- 18. Alonso EE. Triggering and motion of landslides. Géotechnique. 2021;71(1):3-59.
- 19. de Borst R. Computational Methods for Fracture in Porous Media: Isogeometric and Extended Finite Element Methods. Elsevier; 2017.
- 20. Khoei AR. Extended Finite Element Method: Theory and Applications. John Wiley & Sons; 2014.
- 21. Song X, Borja RI. Mathematical framework for unsaturated flow in the finite deformation range. *Int J Numer Methods Eng.* 2014;97(9):658-682.
- 22. Song X, Silling SA. On the peridynamic effective force state and multiphase constitutive correspondence principle. *J Mech Phys Solids*. 2020;145(July):104161.
- 23. Menon S, Song X. A computational periporomechanics model for localized failure in unsaturated porous media. *Comput Methods Appl Mech Eng.* 2021;384:113932.
- 24. Menon S, Song X. Computational multiphase periporomechanics for unguided cracking in unsaturated porous media. *Int J Numer Methods Eng.* 2022;123(12):2837-2871.
- 25. Menon S, Song X. A stabilized computational nonlocal poromechanics model for dynamic analysis of saturated porous media. *Int J Numer Methods Eng.* 2021;122(20):5512-5539.
- 26. Menon S, Song X. Shear banding in unsaturated geomaterials through a strong nonlocal hydromechanical model. *European Journal of Environmental and Civil Engineering*. 2020;26(8):3357-3371.
- 27. Coussy O. Poromechanics. John Wiley & Sons; 2004.
- 28. Cheng AH. A linear constitutive model for unsaturated poroelasticity by micromechanical analysis. *Int J Numer Anal Methods Geomech*. 2020;44(4):455-483.
- 29. Lu N, Likos W. Unsaturated Soil Mechanics. John Wiley&Sons; 2004.
- 30. Silling SA, Epton M, Weckner O, Xu J, Askari E. Peridynamic states and constitutive modeling. J Elast. 2007;88(2):151-184.
- 31. Madenci E, Oterkus E. Peridynamic Theory and Its Applications. Springer; 2014.
- 32. Silling SA. Stability of peridynamic correspondence material models and their particle discretizations. *Comput Methods Appl Mech Eng.* 2017;322:42-57.
- 33. Menon S, Song X. Updated Lagrangian unsaturated periporomechanics for extreme large deformation in unsaturated porou media. *Comput Methods Appl Mech Eng.* 2022;400:115511.https://doi.org/10.1016/j.cma.2022.115511.

- 34. Fredlund DG, Rahardjo H. Soil Mechanics for Unsaturated Soils. John Wiley & Sons; 1993.
- 35. Chowdhury SR, Roy P, Roy D, Reddy J. A modified peridynamics correspondence principle: removal of zero-energy deformation and other implications. *Comput Methods Appl Mech Eng.* 2019;346:530-549.
- 36. Ng CWW, Menzies B. Advanced Unsaturated Soil Mechanics and Engineering. CRC Press; 2014.
- 37. Gabriel E, Fagg GE, Bosilca G, et al. Open MPI: goals, concept, and design of a next generation MPI implementation. Proceedings of the European Parallel Virtual Machine/Message Passing Interface Users' Group Meeting; 2004:97-104; Springer.
- 38. Zienkiewicz O, Paul D, Chan A. Unconditionally stable staggered solution procedure for soil-pore fluid interaction problems. *Int J Numer Methods Eng.* 1988;26(5):1039-1055.
- 39. Simoni L, Schrefler B. A staggered finite-element solution for water and gas flow in deforming porous media. *Commun Appl Numer Methods*. 1991;7(3):213-223.
- 40. Armero F, Simo J. A new unconditionally stable fractional step method for non-linear coupled thermomechanical problems. *Int J Numer Methods Eng.* 1992;35(4):737-766.
- 41. Turska E, Wisniewski K, Schrefler B. Error propagation of staggered solution procedures for transient problems. *Comput Methods Appl Mech Eng.* 1994;114(1-2):177-188.
- 42. Schrefler B, Simoni L, Turska E. Standard staggered and staggered Newton schemes in thermo-hydro-mechanical problems. *Comput Methods Appl Mech Eng.* 1997;144(1-2):93-109.
- 43. Ni T, Pesavento F, Zaccariotto M, Galvanetto U, Zhu QZ, Schrefler BA. Hybrid FEM and peridynamic simulation of hydraulic fracture propagation in saturated porous media. *Comput Methods Appl Mech Eng.* 2020;366:113101.
- 44. Ni T, Pesavento F, Zaccariotto M, Galvanetto U, Schrefler BA. Numerical simulation of forerunning fracture in saturated porous solids with hybrid FEM/Peridynamic model. *Comput Geotech.* 2021;133:104024.
- 45. Uzuoka R, Borja RI. Dynamics of unsaturated poroelastic solids at finite strain. Int J Numer Anal Methods Geomech. 2012;36(13):1535-1573.
- 46. Silling SA, Parks ML, Kamm JR, Weckner O, Rassaian M. Modeling shockwaves and impact phenomena with Eulerian peridynamics. *Int J Impact Eng.* 2017;107:47-57.
- 47. Silling SA, Askari E. A meshfree method based on the peridynamic model of solid mechanics. Comput Struct. 2005;83(17-18):1526-1535.
- 48. Song X, Wang K, Bate B. A hierarchical thermo-hydro-plastic constitutive model for unsaturated soils and its numerical implementation. *International Journal for Numerical and Analytical Methods in Geomechanics*. 2018;42(15):1785-1805.
- 49. Song X, Khalili N. A peridynamics model for strain localization analysis of geomaterials. *International Journal for Numerical and Analytical Methods in Geomechanics*. 2018;43(1):77-96.
- 50. Song X, Menon S. Modeling of chemo-hydromechanical behavior of unsaturated porous media: a nonlocal approach based on integral equations. *Acta Geotechnica*. 2018;14(3):727-747.
- 51. Van Genuchten MT. A closed-form equation for predicting the hydraulic conductivity of unsaturated soils. *Soil Sci Soc Am J*. 1980;44(5):892-898.
- 52. Cao J, Jung J, Song X, Bate B. On the soil water characteristic curves of poorly graded granular materials in aqueous polymer solutions. *Acta Geotech.* 2018;13(1):103-116.
- 53. Niu WJ, Ye WM, Song X. Unsaturated permeability of Gaomiaozi bentonite under partially free-swelling conditions. *Acta Geotech*. 2020;15(5):1095-1124.
- 54. Wang K, Song X. Strain localization in non-isothermal unsaturated porous media considering material heterogeneity with stabilized mixed finite elements. *Comput Methods Appl Mech Eng.* 2020;359:112770.
- 55. Song X, Ye M, Wang K. Strain localization in a solid-water-air system with random heterogeneity via stabilized mixed finite elements. *Int J Numer Methods Eng.* 2017;112(13):1926-1950.
- 56. Likos WJ, Song X, Xiao M, Cerato A, Lu N. Fundamental Challenges in Unsaturated Soil Mechanics. Springer Series in Geomechanics and Geoengineering. 2019;209-236. doi:10.1007/978-3-030-06249-1_8
- 57. Zhang Z, Song X. Soil-water retention surface of unsaturated clay incorporating capillary interface area through molecular dynamics. *Geo-Congress* 2022. 2022:1-10. doi:10.1061/9780784484050.034
- 58. Zhang Z, Song X. Nanoscale soil-water retention curve of unsaturated clay via MD and machine learning. *arXiv*. 2021:1-15. doi:10.48550/ARXIV.2201.04949
- $59. \ \ Song\ X,\ Borja\ RI.\ Finite\ deformation\ and\ fluid\ flow\ in\ unsaturated\ soils\ with\ random\ heterogeneity.\ \textit{Vadose}\ Zone\ J.\ 2014;13(5):1-11.$
- 60. Song X. Transient bifurcation condition of partially saturated porous media at finite strain. *Int J Numer Anal Methods Geomech*. 2017;41(1):135-156.
- 61. Hughes TJ. The Finite Element Method: Linear Static and Dynamic Finite Element Analysis. Courier Corporation; 2012.
- 62. Borja RI, Kishnani SS. On the solution of elliptic free-boundary problems via Newton's method. *Comput Methods Appl Mech Eng.* 1991;88(3):341-361.
- 63. Menon S, Song X. Coupled analysis of desiccation cracking in unsaturated soils through a non-local mathematical formulation. *Geosciences*. 2019;9(10):428.
- 64. Hill R. A general theory of uniqueness and stability in elastic-plastic solids. J Mech Phys Solids. 1958;6(3):236-249.
- 65. Kakogiannou E, Sanavia L, Nicot F, Darve F, Schrefler BA. A porous media finite element approach for soil instability including the second-order work criterion. *Acta Geotech.* 2016;11(4):805-825.
- 66. del Castillo EM, Neto AHF, Borja RI. A continuum meshfree method for sandbox-style numerical modeling of accretionary and doubly vergent wedges. *J Struct Geol.* 2021;153:104466.

- 67. del Castillo EM, Fávero Neto AH, Borja RI. Fault propagation and surface rupture in geologic materials with a meshfree continuum method. *Acta Geotech.* 2021;16(8):2463-2486.
- 68. Trifunac M, Hudson D. Analysis of the Pacoima dam accelerogram—San Fernando, California, earthquake of 1971. *Bull Seismol Soc Am.* 1971;61(5):1393-1411.
- 69. Seed HB, Idriss IM, Lee KL, Makdisi FI. Dynamic analysis of the slide in the Lower San Fernando Dam during the earthquake of February 9, 1971. *J Geotech Eng Div.* 1975;101(9):889-911.

How to cite this article: Menon S, Song X. Computational coupled large-deformation periporomechanics for dynamic failure and fracturing in variably saturated porous media. *Int J Numer Methods Eng.* 2022;1-39. doi: 10.1002/nme.7109